

AD-A095 893

IMPERIAL COLL OF SCIENCE AND TECHNOLOGY LONDON (ENGLA--ETC F/6 21/7
VELOCITY CHARACTERISTICS OF THE FLOW IN MOTORED ENGINES.(U)
JUN 80 C ARCOUMANIS, A F BICEN, A D GOSMAN DA-ERO-79-6-0030

UNCLASSIFIED

NL

1 of 1
AD-A095 893

END
DATE
FILMED
4-81
DTIC

LEVEL

12

AD A 095893

DTIC
ELECTE
S MAR 4 1981 D
A



Imperial College

Department of
Mechanical
Engineering

This document has been approved
for public release and sale in
distribution is unlimited.

FILE COPY

81 3 2 103

VELOCITY CHARACTERISTICS OF THE FLOW
IN MOTORED ENGINES

by

C. Arcoumanis, A.F. Bicen,
A.D. Gosman, A.P. Morse and J.H. Whitelaw

June, 1980

EUROPEAN RESEARCH OFFICE

United States Army

London England

GRANT NUMBER DA-ERO-79-G-0030

Imperial College of Science and Technology
London SW7 2AZ, England

Approved for Public Release; distribution unlimited

UNCLASSIFIED

R&D 2635-AN

SECURITY CLASSIFICATION OF THIS PAGE (When Data Entered)

REPORT DOCUMENTATION PAGE		READ INSTRUCTIONS BEFORE COMPLETING FORM
1. REPORT NUMBER	2. GOVT ACCESSION NO.	3. RECIPIENT'S CATALOG NUMBER
	AD-A095 893	7
4. TITLE (and Subtitle)		5. TYPE OF REPORT & PERIOD COVERED
VELOCITY CHARACTERISTICS OF THE FLOW IN MOTORED ENGINES.		Final Technical Report, April 1979-June 1980
6. AUTHOR(s)		7. PERFORMING ORG. REPORT NUMBER
C. /Arcoumanis / A.F. /Bicen / A.D. /Gosman A.P. /Morse and J.H. /Whitelaw		
8. CONTRACT OR GRANT NUMBER(s)		
DA-ERO-79-6-0030		
9. PERFORMING ORGANIZATION NAME AND ADDRESS		10. PROGRAM ELEMENT, PROJECT, TASK AREA & WORK UNIT NUMBERS
Imperial College of Science and London SW7 2AZ, England Technology		6.11.02A 1T161102BH57-06
11. CONTROLLING OFFICE NAME AND ADDRESS		12. REPORT DATE
European Research Office, United States Army, London, England		11 June 1980
13. MONITORING AGENCY NAME & ADDRESS (if different from Controlling Office)		13. NUMBER OF PAGES
51		53
14. SECURITY CLASS. (of this report)		
Unclassified		
15. DECLASSIFICATION/DOWNGRADING SCHEDULE		
16. DISTRIBUTION STATEMENT (of this Report)		
Approved for Public Release; distribution unlimited		
17. DISTRIBUTION STATEMENT (of the abstract entered in Block 20, if different from Report)		
18. SUPPLEMENTARY NOTES		
19. KEY WORDS (Continue on reverse side if necessary and identify by block number)		
Flow in engines Velocity measurements Laser-Doppler anemometry		
20. ABSTRACT (Continue on reverse side if necessary and identify by block number)		
Measurements of mean and rms values of axial velocity, obtained with a laser anemometer, are reported for a swirling incompressible air flow in a piston-cylinder assembly motored at 200 rpm to quantify the influence of stroke and clearance. The results show that longer stroke causes the formation of stronger vortices cont.		

DD FORM 1473
1 JAN 73

EDITION OF 1 NOV 53 IS OBSOLETE

UNCLASSIFIED

SECURITY CLASSIFICATION OF THIS PAGE (When Data Entered)

47-2111 → 72

UNCLASSIFIED

SECURITY CLASSIFICATION OF THIS PAGE(When Data Entered)

20. while smaller clearance generates higher turbulence levels at the early part of the intake stroke; in both cases vortices decay as the piston approaches BDC.

Measurements of swirl velocities are also reported in a Diesel engine motored at 675 rpm with compression and 500 rpm without compression to quantify the influence of compression. The results show that the influence is insignificant in the intake stroke and the beginning of the compression stroke, but at higher crank angles the flow, under compression, tends towards solid body rotation.

The experimental results in the non-compressing engine are compared with calculations obtained by numerical solution of the conservation equations and show that the major flow features are correctly predicted.

B

UNCLASSIFIED

SECURITY CLASSIFICATION OF THIS PAGE(When Data Entered)

ABSTRACT

Measurements of mean and rms values of axial velocity, obtained with a laser anemometer, are reported in a piston cylinder assembly motored at 200rpm, in the absence of compression. The inlet arrangement consisted of a simulated open valve inclined at 60° to the cylinder head and incorporated 30° swirl vanes which provided a swirl number of about 1.2. Results, obtained with a flat piston and a 90mm stroke, are compared to those with a 60mm stroke reported elsewhere. In addition to the bore to stroke ratio influence, the influence of clearance volume is investigated by comparing results for two different clearance distances of 30mm and 10mm. The results show that longer stroke causes the formation of stronger vortices while smaller clearance generates higher turbulence levels at the early part of the intake stroke; in both cases vortices decay as the piston approaches BDC.

Measurements of swirl velocity are also reported in a single-cylinder Diesel engine motored at 675 rpm to quantify the influence of compression. The results show close correspondence with the non-compressing results at 500rpm in the intake stroke and the beginning of the compression stroke. At higher crank angles the flow tends towards solid body rotation.

The experimental results in the non-compressing engine are compared with calculations obtained by numerical solution of the conservation equations and show that the major flow features are correctly predicted.

✓
A

1. Introduction

In a series of recent papers, the in-cylinder velocity characteristics of motored piston-cylinder arrangements have been documented. These results were obtained with open-port configuration and, therefore, without compression or combustion, and quantify the flow patterns for a series of axisymmetric port arrangements (1 to 5) and for an off-centre port (6). Preliminary measurements in a motored, single-cylinder engine have also been reported (7) and were considerably more difficult to obtain than in the perspex arrangement of the previous references. The purposes of the work are to quantify the influence of the various flow and geometry boundary conditions present in internal combustion engines and so to improve understanding of the related mechanisms and to provide a basis for the evaluation of detailed design methods.

The present report focuses on those aspects of the programme described above which relate to Grant DA-ERO-79-G-0030, namely explorations of the effect of swirl and piston bowls in the in-cylinder air flow. Also measurements are reported on the influence of bore to stroke ratio and clearance volume in the non-compressing engine for an open valve incorporating swirl vanes and of compression in a motored single-cylinder Diesel engine.

The experimental work in the non-compressing engine was undertaken in conjunction with calculations which were obtained by the solution of conservation equations in finite-difference form. The calculated results presented here are intended to allow evaluation of the calculation method; previous work of this type has been reviewed in references 8 and 12.

2. Flow configurations and measurement methods

The model engine comprised a plexiglass piston reciprocated in a plexiglass cylinder of 75mm diameter, in simple harmonic motion, by a motor and crank arrangement at a speed of 200 rpm. For the present measurements, the flat piston had a stroke of 90mm with clearance distances of 10 and 30mm. An open annular port angled at 60 degrees to the plane of the cylinder head and with a 4mm gap, was located centrally in the cylinder head. An arrangement of 30 degrees swirl vanes located upstream of the port gave rise to a swirl number of around 1.2. The flow was seeded with atomised silicone oil.

The single-cylinder Petter Diesel compressing engine was motored at speeds up to 675 rpm. Measurements were obtained at compression ratios of 17.5 and zero, the exhaust valve being held open with a constant lift of 0.63mm to ensure the zero compression condition. The injection equipment was removed

and replaced by a quartz window with an effective diameter of 41 mm which allowed optical access to the cylinder.

Figure 1 provides a line diagram of the instrumentation used to obtain measurements in the model engine. It comprised a 5mW helium-neon laser, a rotating diffraction grating, three focussing lenses, a light-collecting lens and a photomultiplier with a pinhole which controlled the diameter of the probe volume. The arrangement is similar to that used, and described in greater detail, in references 1 to 3. For the present measurements, the main optical characteristics were:

half angle of intersecting beams	6.4 degrees
fringe spacing	2.8 μm
frequency-to-velocity, with 1.83MHz shift	2.8 $\text{ms}^{-1}/\text{MHz}$
effective diameter of measuring volume	$\sim 100 \mu\text{m}$
effective length of measuring volume	$\sim 1.03 \text{ mm}$

The Doppler signals from the photomultiplier were band-pass filtered, amplified and input to a frequency counter and oscilloscope. The filter had a flat response between 0.27 MHz and 4.1 MHz, corresponding to the range of velocities expected. The triggering mechanism of the oscilloscope was used to accept Doppler signals above a certain threshold level and, for each corresponding burst, an arming pulse was sent from the oscilloscope to the measuring time input of the counter. The start and stop information of the arming pulses, allowed by the 3ms response of the counter (which permitted a maximum of about 100 samples per revolution) was sent to a 'gating' circuit. The latter also received a train of 1,000 pulses per revolution and a marker pulse at top-dead-centre (TDC) from an optical shaft encoder coupled to the engine drive shaft and synchronized with its rotation.

The binary-coded, decimal frequency outputs from the counter and encoder, were interfaced to a microprocessor (Apple II) and stored in memory. The data acquisition was controlled by assembly long-range software and the data analysis performed by Basic language software. For each crank-angle window, in the present case 10 degrees was used, the ensemble-averaged velocities and the rms of the velocity fluctuations were calculated after those points greater than three standard deviations from the mean value had been rejected. The velocity histogram was also calculated and monitored for spurious effects. The resulting ensemble averages were transferred to a mainframe computer (CDC 6500) and the pro-

files and streamlines plotted; the streamlines were obtained by linear interpolations.

The optical arrangement used for measurements in the Petter engine operated with back-scattered light and made use of an argon-ion laser with a double-Bragg cell optical arrangement. It is described in preliminary form in reference 9 and in present form in reference 10. The main optical characteristics were:

half angle of intersecting beams	5.7 degrees
fringe spacing	2.44 μm
frequency-to velocity, with +2.5 MHz shift	2.44 $\text{ms}^{-1}/\text{MHz}$
effective length of measuring volume	0.5 mm
effective diameter of measuring volume	52 μm

The signal-processing arrangement, described in connection with the plexiglass engine, was also used to process the signals from the Petter engine.

The accuracy of the measurements in both engine arrangements have been discussed at length in the various references quoted. For present purposes, it is sufficient to comment that the physical conclusions which can be drawn from the results are not limited by measurement accuracy.

3. Calculation method

Basic Equations. Like others of its kind, the multi-dimensional 'RPM' (standing for 'Reciprocating Piston Motion') method, used for the computer simulations, operates by solving the governing differential conservation equations of mass, momentum, energy etc. numerically by finite-difference means.

In order to make such an approach feasible, it is necessary to formulate the equations in ensemble-average form, in which the dependent variables represent, at a given crank angle in the engine cycle, the mean behaviour averaged over many such cycles. This is analogous to the time-averaging process when applied to steady flows and gives rise to conservation equations of the form (reference 15), in Cartesian tensor notation:

$$\frac{\partial \rho}{\partial t} + \frac{\partial}{\partial x_i} (\rho U_i) = 0 \quad (1)$$

$$\frac{\partial (\rho U_i)}{\partial t} + \frac{\partial}{\partial x_j} (\rho U_j U_i - \mu E_{ij}) = - \frac{\partial}{\partial x_j} (\overline{\rho u_i' u_j'}) - \frac{\partial p}{\partial x_i} + S_u \quad (2)$$

$$\frac{\partial(\rho h)}{\partial t} + \frac{\partial}{\partial x_j} (\rho U_j h - \overline{\rho u_j' h'}) = - \frac{\partial}{\partial x_j} (\overline{\rho u_j' h'}) + S_h \quad (3)$$

where U_i is the ensemble-averaged velocity in direction x_i , p stands for pressure, $h (\equiv C_p T + \frac{1}{2} U_i U_i + k)$ is the stagnation enthalpy and the remaining symbols have their usual significance.

The terms $\overline{\rho u_i' u_j'}$ and $\overline{\rho u_j' h'}$ appearing in the above equations are additional unknowns arising from the ensemble-averaging process and represent, respectively, turbulent fluxes of momentum and energy. These must be connected, via additional equations, to variables which are either known or calculable, an activity which has come to be known as 'turbulence modelling' and which represents one of the major areas of uncertainty in the ensemble-average formulation. Space does not allow the various alternative models and their pros and cons to be discussed here, but references 11 and 13 can be consulted. All that will be said is that, after due consideration, the model employed for all RPM applications to date relates the turbulent fluxes to the mean flow properties via:

$$-\overline{\rho u_i' u_j'} = \mu_t \left(\frac{\partial U_i}{\partial x_j} + \frac{\partial U_j}{\partial x_i} \right) - \frac{2}{3} \delta_{ij} \left(\mu_t \frac{\partial U_j}{\partial x_j} + \rho k \right) \quad (4)$$

$$-\overline{\rho u_j' h'} = \frac{\mu_t}{\sigma_h} \frac{\partial h}{\partial x_j}$$

where the turbulent viscosity μ_t is a function of the local ensemble-averaged turbulence energy k and its dissipation rate ϵ thus:

$$\mu_t = C_\mu \rho k^{3/2} / \epsilon \quad (6)$$

and the latter quantities are obtained from their own differential transport equations, which run:

$$\frac{\partial}{\partial t} (\rho k) + \frac{\partial}{\partial x_j} (\rho U_j k - \frac{\mu_t}{\sigma_k} \frac{\partial k}{\partial x_j}) = G_t - \rho \epsilon + S_k \quad (7)$$

$$\frac{\partial}{\partial t} (\rho \epsilon) + \frac{\partial}{\partial x_j} (\rho U_j \epsilon - \frac{\mu_t}{\sigma_\epsilon} \frac{\partial \epsilon}{\partial x_j}) = \frac{\epsilon}{k} (C_1 G_t - C_2 \rho \epsilon) + S_\epsilon \quad (8)$$

Here the quantities C_μ , C_1 , C_2 etc. represent empirical coefficients whose values have been fixed by earlier investi-

gators by reference to simpler flows.

When chemical reaction is involved, as in the combustion process, similar equations to the above can be derived for the 'mean' and turbulent properties of the species concentration fields, as described in reference 14 and elsewhere.

Transformed Equations. For reasons of convenience and economy, the differential equations are recast from the Eulerian Cartesian coordinate frame into a general mixed Eulerian/Lagrangian curvilinear-orthogonal frame which, as the term implies, can be caused to locally move in any prescribed fashion in relation to the fluid, within the constraint that the frame must remain single-valued and orthogonal. The moving-frame feature is introduced so as to allow for the motion of the piston and valves, while the flexibility of the curvilinear-orthogonal framework permits it to accommodate to the often-complex shape of the chamber walls.

The resulting equations have the general form:

$$\frac{1}{L} \frac{\partial}{\partial t} (L \rho \phi) + \nabla \cdot (\rho \vec{U} \phi - \frac{\Gamma_{\phi}}{l_j} \frac{\partial \phi}{\partial \xi_j}) - S_{\phi} = 0 \quad (9)$$

where: \vec{U} is the velocity vector relative to the moving frame, having components U_i in directions ξ_i ; ϕ stands for any of the dependent variables and Γ_{ϕ} and S_{ϕ} the associated 'diffusion' and 'source' coefficients; the l_j are time-varying metric coefficients connecting increments in the ξ_i with those in physical space; $L \equiv l_1 l_2 l_3$ and

$$\nabla \cdot \equiv \frac{1}{L} \frac{\partial}{\partial \xi_j} (l_m l_n) \quad j \neq m \neq n \quad (10)$$

The boundary conditions on these and the other equations of the complete set are imposed, for reasons of economy, indirectly through the now-common device of 'wall functions', in this instance based on the theory of steady one-dimensional boundary layers; it should be remarked that here too the price of economy is additional uncertainty, in this case about the validity of this particular boundary-layer model in engine circumstances.

Further details of the forms which the individual equations take under the above transformation can be found in reference 15, if desired. The manner in which the flexibility which it offers is exploited will now be explained.

Finite-difference grid and equations. The grid configuration for the present calculations is shown in Figure 2. The nominally cylindrical-polar grid in the clearance space between the piston crown and cylinder head is caused to axially expand and contract with the piston motion, in a concertina fashion. The grid within the piston bowl, where present, simply translates with it. This is arranged to occur through appropriate specification of the ξ 's and metric coefficients and effectively results in the complex-geometry, moving - boundary problem being transformed into a fixed rectilinear region in ξ space. As a consequence differencing techniques originally developed for Eulerian problems may be applied with only modest modification.

As documented in references 11 and 16, the finite-difference counterparts (fdes) of the parent transformed differential equations are derived by integration, with the aid of approximations, over imaginary control volumes enclosing each grid intersection or 'node'. The result is, for a typical node 'p' of the grid:

$$a_p \phi_p^N = \sum A_n \phi_n^N + S_p^N + A_p^{OO} \phi_p^O \quad (11)$$

where the summation is over the neighbouring pairs of nodes in the positive and negative, ξ_1 , ξ_2 and ξ_3 (i.e. circumferential) directions, and the 'N' and 'O' superscripts denote 'new' and 'old' values separated by a finite time interval δt . The A's express the combined effects of convection and diffusion, here approximated by a hybrid central/upwind difference formulation and A_p^N represents the integrated source. The appearance of N 's p on the right-hand side of eqn (11) indicates that the formulation is implicit in time and therefore requires solution of simultaneous algebraic equations at each new time interval. How this is accomplished will now be outlined.

Solution algorithm. Starting from initial prescriptions of the distributions of the velocities, pressures, temperature etc. within the chamber (which of course will influence only the 'start-up' phase of the engine simulation and not the steady operating condition) the method advances in discrete intervals of crank angle. At each interval the distributions are updated by iterative, simultaneous solution of the coupled difference equations for the variables, with appropriate adjustments to the grid and coefficients to allow for the piston displacement and such events as valve movement, fuel injection, ignition etc,. In the present application, the pressure drop across the permanently-open valve is negligible and the flow through it is simply calculated as

though it were incompressible, on the assumption that it enters at the valve seat angle with plug profiles of all velocity components and negligible turbulence level.

The iteration sequence commences by making estimates of the overall temperature and pressure levels via global conservation equations derived from the fdes. The local velocities are then estimated by solution of the momentum equations using an Alternating-Direction Implicit ('ADI') procedure, following which they are adjusted to satisfy local continuity requirements via a continuity-based pressure field calculation. The remaining variables are then calculated in turn and the whole sequence is repeated until all equations are brought into balance.

4. Results

4.1 Measurements

Detailed descriptions of the experimental results obtained from the non-compressing engine in the presence of a cylindrical piston bowl and/or swirl are available in references 2 and 3 respectively. Accordingly, in what follows, more recent explorations into the effects of bore to stroke ratio, clearance volume and compression will be described.

Ensemble-averaged mean and rms velocity values were obtained in the model engine for two bore:stroke ratios and corresponding contours of the stream function are presented in Figures 3 to 8 for crank angles of 36, 90, 144, 170, 190 and 200 degrees after top-dead-centre (ATDC). The effect of piston stroke can be determined by comparing the results with the 90mm stroke and 30mm clearance with those of Figure 17 and reference 5 which were obtained at the same rotational speed of 200 rpm and the same clearance of 30mm but with a stroke of 60mm; these two arrangements correspond to bore-to-stroke ratios of 1.25 and 0.83 respectively. A more extensive description of these results will appear in reference 17.

The results of Figure 3 show similar flow patterns in the two clearance volumes but with the centre of the annular vortices closer to the cylinder head for the smaller clearance. In both cases, the main annular vortex circulates about 40% of the total mass flow rate but the corner vortex is much stronger with the smaller clearance and circulates about 50% of the mass flow rate compared with 20% for the larger clearance. Comparison with the results of Figure 17

obtained with the 60mm stroke shows that both the main and the corner vortices are stronger with the longer stroke and circulate almost double the mass. As a consequence no vortex is formed between the axis and the cylinder head.

Figure 4 shows the streamline patterns at mid-stroke. As in the previous case of 36° crank angle the flow patterns are similar but the main vortex extends more towards the piston face for the smaller clearance; it circulates about 120% of the total mass flow rate compared to the 100% with the larger clearance. The newly-formed vortices between the axis and the cylinder head are of equal strength circulating only 2% of the mass flow rate while the corner vortices are stronger and circulate each about 25% of the net mass. Comparison with the 60mm stroke results shows very similar flow patterns with the three vortices in the shorter stroke case being slightly weaker by no more than 10%.

Figure 5 presents streamline patterns at 144° crank angle; the similarities still exist with the only difference the formation of a small vortex between the wall and the piston which circulates not more than 5% of the total mass flow rate. The trends observed at midstroke with respect to the strength of the other three vortices are repeated here; the main vortex is stronger with the smaller clearance and circulates about 110% of the mass flow rate compared to 80% for the large one, while the other two smaller vortices are of equal strength in the two cases. Comparison with the flow pattern obtained with the 60mm stroke (Figure 17) reveals that although the centres of the main vortices are located in the same axial distance from the cylinder head, the main vortex is much stronger with the shorter stroke and circulates about 180% of the total mass flow rate compared with 80% for the 90mm stroke; similar trends are observed with the corner vortices.

The results presented in Figure 6 show that the main vortices remain stationary with respect to their position at 144° crank angle and do not follow the piston motion towards BDC. The trend in their strength is opposite to that observed at previous crank angles; the main vortex with the smaller clearance is much weaker now and circulates about 180% of the total mass flow rate compared to 300% with the 30mm clearance. A new vortex is formed between the wall and the piston in the case of the larger clearance and circulates more than 100% of the total mass compared to 25% for the one with the smaller clearance which was present in the previous crank angle. However, in the latter case the main vortex breaks up and forms a very weak vortex near the cylinder

axis. Comparison with the results for the 60mm stroke shows that the flow patterns are very similar with the main vortices occupying the same space and circulating approximately the same total mass flow rate; this is not true for the corner vortices with the one at 60mm stroke circulating around 130% compared to 50% with the longer stroke.

The flow patterns presented in Figure 7 show distinct similarities. The main vortices have been squeezed towards the wall and reduced considerably in size while the vortices formed between the wall and piston have grown up and pushed towards the axis. The latter vortex with the larger clearance circulates about 50% of the mass flow rate compared to 30% for the smaller clearance; the main vortices are of equal strength and circulate at 190° crank angle only 40% of the total mass compared to 180% and 300% for the larger and shorter clearances at $\theta = 170^\circ$. Comparison with the results of reference 5 for the shorter stroke shows that in this case the main vortex remains appreciable in size and circulates more than 100% of the total mass compared to the 40% with the 90mm stroke. The vortex, formed between the wall and the piston at 170° crank angle with the shorter stroke, breaks up forming a small one near to the axis which does not exist in the longer stroke case.

Figure 8 presents flow patterns obtained at 200° crank angle. The similarities still exist with all the vortices being destroyed by the sweeping action of the returning piston except the one close to the axis; this vortex is larger with the smaller clearance and circulates 10% of the total mass compared to 1% for the 30mm clearance. Comparison with the flow patterns obtained with the 60mm stroke reveals that in the case of longer stroke the system of vortices is destroyed earlier; the main vortex is still present in the shorter stroke case and circulates about 40% of the total mass.

Measured values of the mean circumferential velocity, obtained in the single cylinder Petter engine, are shown in Figure 9. They correspond to a rotational speed of 675 rpm with compression and 500 rpm without, to the plane 10mm below the cylinder head and to five crank-angle values, each with and without compression. Measurements of the rms of the velocity fluctuations at the same locations were obtained and are reported, together with additional velocity values and a more complete description, in reference 10. The non-compressing flow was obtained by keeping the exhaust valve open, with a constant lift of 0.63mm, throughout the cycle.

It can be deduced from Figure 9 that the mean velocity characteristics are similar with and without compression. There are small differences in the magnitudes and locations of the velocity maxima and minima but these are slight and confirm the expected small influence of the open exhaust valve. In general, the flow is characterised by a region of high velocity near the cylinder wall, corresponding to the strongly spiralling jet induced by the masked inlet valve. The peak jet velocity, obtained near mid-stroke, is of the order of seven times the mean piston speed and lies very close to the cylinder wall. There is also a region of low swirl velocity, away from the wall and corresponding to the wake formed behind the stem of the valve. By mid-stroke, this wake has decreased considerably in strength and continues to do so as the stroke continues.

Past bottom-dead-centre, compression has an increasing influence. For the compressing measurements, the inlet valve remains open to 215 degrees and, on closing, the centre of rotation moves rapidly away from the cylinder axis and towards the axes of the valves. Thereafter, the centre of rotation again moves towards the cylinder axis and becomes increasingly symmetrical. Without compression, the symmetric solid-body rotation characteristic of the compression stroke is destroyed and the centre of the flow rotates more rapidly and, by 240 degrees, more rapidly than the outer region. As the piston approaches top-dead centre, the flow is forced into the piston bowl and gives rise to swirl velocities which are higher without compression at 300 degrees. After 330 degrees (not shown) the non-compressing circumferential velocities in the bowl decelerate rapidly whereas, with compression, the velocities increase by a factor of four with the rotation centred at the axis. The corresponding maximum radial velocity at 330 degrees was of the order of four times the mean piston speed.

4.2 Calculated results

In this section, selected measurements from the non-compressing engine are compared with computer predictions obtained with the 'RPM' method. In the first instance, data for a case having no swirl or piston bowl are presented, to serve as a benchmark; then two further cases are described where one or the other of these features is present.

All calculations were performed on grids having the general arrangement of Figure 2 and with a crank-angle interval of 2°. The no swirl cases were found to be free from start-up effects after the first cycle, while the swirling case

required three cycles to reach this state.

4.2.1 Case 1- Flat Piston, No Swirl

Figure 10 shows the predicted velocity field in the form of velocity vectors* at 36° , 90° , 144° and 270° ; the corresponding experimental streamlines are shown in Figure 11.

At 36° , the overall flow structure is reasonably well predicted. Specifically, areas of agreement are: the existence and correct sense of rotation of the recirculation zones centred at (a) and (b); the position on the centre of (b); and the location of the stagnation point on the axis. Features not predicted so well are the position of the centre of vortex (a) and its axial extent, the discrepancies in the calculation apparently being caused by higher radial velocities immediately downstream of the inlet.

The experimental and predicted flow fields at the mid-stroke position (90°) show slightly better agreement in respect of the length of vortex (a). The eddy centred at (b) is also well-predicted, although at (c) the small recirculation zone observed in the measurements has not appeared in the predictions.

Agreement is better at 144° at (c) although the measurements indicate a larger recirculation zone (examination of the numerical values of the predictions shows only small negative axial velocities adjacent to the wall at (c)). Other features of the flow including the vortices at (a) and (b) are generally in good agreement.

At the mid-stroke position during exhaust (270°) the sink-line appearance of the flow is well-predicted, with the exception of a weak residual eddy at (a) which is not seen in the measurements.

* The velocities are plotted in the form of arrows indicating the direction, determined from the resultant of the axial and radial components, whilst their length is scaled linearly with the magnitude. The same scaling is used at each crank-angle and a reference vector is included to indicate the scaling factor.

Figures 12 to 15 show comparisons for the same case between the axial mean (\bar{V}_1) and r.m.s. turbulent ($\overline{v_1'^2}^{1/2}$) velocity profiles, normalised by the mean piston speed, at a number of axial positions and the same crank-angles as previously. At 36° (Figure 12) the axial velocity at $z = 10$ mm is in reasonable agreement with the measurements with coincident radial positions of the peak at $r = 24$ mm, although the level is under-predicted by about 25%. The peak negative value is 40% higher than that measured at $r = 15$ mm but is in better agreement nearer to the axis. The peak turbulence intensity is 30% lower than the measurements and the predicted profile is much flatter due, no doubt, in part to the smaller velocity gradients, and hence turbulence generation, in the calculated flow.

At $z = 20$ mm, the predicted axial velocity shows a relatively slow profile for $r > 22$ mm and the negative velocities close to the wall ($r > 30$ mm) evidenced in the measurements are not predicted at all (hence the under-prediction of the length of the recirculation zone (a) in Figure 10). The difference between the measured and predicted profiles suggests that the former retains a jet-like structure for a greater distance than the latter. The turbulence profiles show the calculated values to be about 50% of the measured ones at $r = 23$ mm, although for $r > 15$ mm both mean and turbulent velocities are in better agreement. At $z = 30$ mm, the comparison is considerably better than nearer to the cylinder head, probably because the flow close to the piston is influenced more by the piston motion than by the inlet jet.

At 90° (Figure 13), the peak inlet velocity at $z = 10$ mm is again under-predicted, in this instance by about 30%. Towards the axis ($r > 15$ mm) the measured negative axial velocities are not reproduced. The turbulent velocity shows a flatter profile than the measurements, the latter reflecting the jet-like structure and steeper gradients of the mean velocity. At $z = 20$ mm the positions of the mean velocity peaks in both measurements and predictions have shifted radially outward by about 4 mm and the level of agreement is about the same as at $z > 10$ mm. The measured peak turbulence level close to the wall is not predicted at all and the differences are substantial for $r > 17$ mm. In view of the discrepancies at $z = 10$ mm and $z = 20$ mm, the mean velocity agreement at $z = 30$ mm is surprisingly good, the peak values differing by about 15% with a similar level of agreement for $r > 23$ mm. The turbulence levels are again poorly pre-

dicted however, being only about 30% of the measured values. Bearing in mind the poor upstream correlation, this is not unexpected. The position of the peak mean velocity at $z = 40$ mm shows the predictions to have a higher axial component nearer the wall. This is again evidenced at $z = 50$ mm where a negative axial velocity is observed in the measurements, signalling the existence of the recirculation zone at (c) in Figure 10 that does not appear in the predictions until later in the cycle.

At 144° (Figure 14) the $z = 10$ mm mean velocity profile shows the predicted position of the peak to be much nearer the wall than in the measurements and the negative axial velocities adjacent to the wall in the latter are not apparent, although towards the axis ($r < 15$ mm) agreement is better. The turbulence velocity peak at $r = 24$ mm is under-predicted by 50% but for $r < 20$ mm agrees well; the peak is within 5% and for $r < 20$ mm differences of the order 15% are observed. The two small turbulence peaks between $r = 20$ mm and the wall are not apparent in the predictions although agreement is good for $r < 20$ mm. The $z = 30$ mm mean profile does not correspond to that measured and although the position of zero axial velocity at $r = 22$ mm is coincident, the errors in the positive and negative values either side are between 20% and 50%. The turbulence maxima for $r > 20$ mm are not predicted although at the inner radii agreement is better. At $z = 40$ mm errors in the peak mean velocity at $r = 30$ mm and at the axis are about 25%. The measured turbulence shows high values adjacent to the wall which are not apparent in the calculated profiles past $z = 40$ mm. At $z = 50$ mm, although there are differences in mean velocity at $r = 18$ mm, the peak at $r = 28$ mm and the centreline value agree well. The negative velocity adjacent to the wall at $z = 60$ mm and $z = 70$ mm is under-predicted; thus the strength of the predicted recirculation at (c) in Figure 10 is weaker than that measured.

At the mid-stroke position (270°) during exhaust (Figure 15) errors in the mean velocity peak of the $z = 10$ mm profile are about 25%, increasing to 50% at the axis. The flow is virtually one-dimensional and the level of agreement for both mean and turbulent velocities improves progressively nearer the piston.

4.2.2 Case 2 - Flat Piston, with Swirl

This case corresponds to the measurements for an inlet swirl number S of 1.2 reported in reference 3. The inlet swirl profiles were, in the absence of better information, taken from the measured profiles at a distance of 0.5 mm from the cylinder head, linearly interpolated in time where necessary.

Figure 16 shows the predicted flow structure for comparison with the experimental streamlines of Figure 17. At 36° , the eddies at (a) and (b) are similar to the predictions without swirl, although there are differences near the piston at the region (d) where the large vortex centred at (b) is distorted by swirl. The predicted axial length of recirculation zone (a) is in better agreement than for the no-swirl case, although at (e), the weak vortex observed in the measurements is not apparent. At 90° , the distortion of vortex (b) near the piston at (d) is well predicted although the weak but large measured eddy at (e) is hardly discernable in the calculations. At 144° , the predicted overall structure is similar although "stretched" and agreement is good apart from region (e). It is interesting that the absence of the weak recirculation observed at (c) in the no-swirl case is correctly predicted. The flow at 270° is virtually one-dimensional except close to the valve and piston for both calculations and measurements.

A detailed comparison between the measured and predicted axial velocity and turbulence intensity profiles is presented in Figures 18 to 21. At 36° (Figure 18) the general level of agreement is similar to the previous case. The velocity peak at $z = 10$ mm is under-estimated by 15% and the reverse flow observed in the measurements from $r = 28$ mm to the wall only extends from $r = 32$ mm in the predictions. At the centreline, a negative velocity is predicted instead of the small positive value measured as already indicated by under-prediction of the vortex length (e) in Figure 16. The calculated turbulence profile shows the now-characteristic flat appearance instead of the well defined peak of the measurements, the maximum of the former being about 60% of the latter. At $z = 20$ mm, the mean velocity agreement is quite good near the axis, although between $r = 20$ mm and the wall the predicted profile is smooth instead of the jet-like appearance of the measurements. The measured and calculated mean velocity profiles are of similar shape at $z = 30$ mm but from $r = 20$ mm to the axis, the latter has a steeper gradient such that the centreline velocity is negative instead of positive. The turbulence profiles here show good correlation.

At the mid-stroke position (Figure 19) agreement of the mean velocity at $z = 10$ mm is poor; the reverse flow adjacent to the wall is not predicted, the peak is under-estimated by some 30% and displaced radially outwards, whilst at the axis, a large negative velocity is predicted instead of a small positive value. The well-defined peak of the measured turbulence is replaced in the predictions by a smooth flat profile although two small maxima at $r = 22$ mm and $r = 34$ mm are evidenced in the latter. The predicted turbulence profiles at $z = 3$ mm show these maxima to be generated near the inlet

and subsequently convected downstream, although the measurements here show only a single maximum. The calculated peak value here is only 20% below that measured. Two well defined maxima are also apparent in the measurements but much further downstream at $z = 20$ mm and their positions correspond to the shear layers on either side of the point of maximum velocity. It would seem that the predicted jet has expanded much more rapidly than the measurements indicate. The mean velocity profile at $z = 30$ mm is in better agreement than at $z = 10$ mm or $z = 20$ mm although the peak is still under-predicted by some 20%. The small measured positive velocity at the centreline indicates that the experimentally observed recirculation zone extends at least 30 mm from the cylinder head whereas the predicted length is less than 10 mm. At $z = 40$ mm and $z = 50$ mm agreement of the mean velocity is good with the exception of the centreline value at the latter position. It is no surprise that the turbulence levels at the outer radii ($r > 15$ mm) are under-predicted in view of the poor upstream correspondence.

At 144° (Figure 20) the mean velocity is in poor agreement with the measurements; the substantial reverse flow of the latter adjacent to the wall is not predicted, the peak jet velocity is only 40% of that measured and displaced radially outwards by 10 mm, whilst the centreline value is twice the magnitude and of opposite sign. The turbulence shows a similarly poor correlation although the profiles at $z = 3$ mm suggest that sufficient turbulence is generated near the valve (the peak is under-estimated by about 20%) but is subsequently either dissipated too rapidly or diffused radially at a greater rate than occurs in the measurements. It appears that the predictions have a higher radial velocity than in the experiments; this is not however due to the swirl as the same trend was in evidence in the no-swirl calculations. Further downstream, the agreement improves and from $z = 50$ mm to $z = 80$ mm the comparison is quite good with the exception of the centreline velocity near the piston. The turbulence shows reasonable correlation for $r < 15$ mm and $z = 40$ mm but agreement is poor at the outer radii where the measurements still show the influence of the intake jet.

Agreement at 270° (Figure 21) is worse than the no-swirl case, with substantially over-estimated velocities for $r < 15$ mm from $z = 20$ mm to $z = 50$ mm. At $z = 3$ mm, where the influence of the valve is strongly felt, the peak mean velocity is over-estimated by 20% but the turbulence is too high by a factor of 4.

Figure 22 shows a comparison between the measured and predicted swirl velocity profiles. The 36° profiles compare favourably with the measurements with errors generally much less than 20% with the exception of the region between $r = 25$ mm and the wall at $z = 10$ mm. At 90° , the effects of the large intake-induced recirculation zone centered at (b) (Figure 16) can clearly be seen in that angular momentum is transported radially inwards to region (d) and the subsequent "spin-up" effect results in peak swirl velocities close to the centreline. Although there are areas of disagreement, notably at $z = 10$ mm and $z = 50$ mm the trends are otherwise surprisingly well predicted. The calculated profiles at $z = 30$ mm and $z = 50$ mm show a greater decay of swirl velocity from $r = 25$ mm to the wall than is measured although this is probably due to the poorly-predicted intake jet. The 144° profiles show better agreement close to the wall but the measurements for $r < 15$ mm at $z = 20$ mm and $z = 30$ mm are only about 50% of those in the calculations. It will be recalled that the predicted axial velocity was in poor agreement in this region, and the high negative values calculated probably account for the increased transport of angular momentum with the associated higher swirl velocities. Near the centreline ($r < 10$ mm) for $z = 50$ mm the measurements show steeper gradients than the calculations. At 270° , agreement is good for all profiles.

4.2.3 Case 3 - Cylindrical Piston Bowl, No Swirl

Predictions are here compared with the data of reference 2 for a simple cylindrical piston bowl inserted in the same configuration as Cases 1 and 2, without swirl. The dimensions of the bowl are shown in Figure 22 and the geometry and operating conditions are otherwise identical to Case 1.

Experimental streamlines are not available for this case and the predicted velocity field, shown in Figure 22, may be compared with the no-bowl calculations of Figure 10. At all crank-angles, the influence of the bowl on the overall flow pattern is seen to be negligible, which is not surprising in view of the absence of compression and the high piston to cylinder-head TDC clearance. It is also noteworthy that the flow within the bowl is relatively unaffected by the intake process and remains one-dimensional throughout the cycle.

A detailed comparison of the axial velocity and turbulence intensity profiles for this case is shown in Figures 24 to 27. Agreement of the mean velocity is worse than the no-bowl case at 36° ; at $z = 10$ mm, the predicted peak value of the intake jet is only 50% of that measured and the reverse flow extending from $r = 29$ mm to the wall is not predicted. The comparison is better near the axis but further downstream at $z = 20$ mm, where the measurements have retained their jet-like appearance, the calculations show a flat profile with no sign of either the peak at $r = 24$ mm or

the negative axial velocities between the centreline and $r = 17$ mm. The turbulence maximum is under-predicted by 40% at $z = 10$ mm although on both sides of the jet, agreement is much better. However, the predicted turbulence decays more rapidly than is indicated by the measurements, a trend also apparent in the previous predictions, such that at $z = 20$ mm; the predicted turbulence level is only 20% of that measured. In the bowl, the mean velocity shows neither axial nor radial variations (with the exception of the gradients at the surface) and the absence of any appreciable stresses near the centre is reflected in low turbulence levels there. Agreement of both mean and turbulent velocities is good at the entrance of the bowl but towards the bottom, calculated values of the latter are only about 30% of the measured ones.

At 90° (Figure 25) agreement of the shape of the mean velocity profile is reasonable at $z = 10$ mm although the peaks of both quantities are under-estimated, in the case of the turbulence, by 50%. Further downstream, the correlation deteriorates; at $z = 30$ mm for example, the peak predicted velocity is only 35% of that measured and the position of the latter is about 5 mm closer to the wall. The position of zero axial velocity is displaced by a similar amount to the peak value and the magnitude of the reverse flow at the centreline is half that of the measurements. The turbulence is also under-predicted and shows a flat profile instead of the double maxima of the measurements. At $z = 50$ mm and $z = 55$ mm, the mean velocity agrees better, probably because this region of the flow is influenced more strongly by the piston motion than the intake jet, although it is still under-predicted, as is the turbulence. In the bowl, agreement is quite good for both quantities, with the essentially one-dimensional velocity profile, as earlier in the cycle, and low turbulence levels.

At 144° (Figure 26) the same comments apply as at 90° . During exhaust (Figure 27) agreement is better than induction with errors in the mean and turbulent velocities up to 25% and 50% respectively.

4.2 Discussion

The foregoing comparisons clearly reveal that, although the predictions mirror fairly well the qualitative features of the in-cylinder motion and the effects thereon of the inlet and piston-geometry alterations explored in the experiments, there exist appreciable quantitative discrepancies in all the cases studied.

It is difficult to pinpoint the causes of the errors because there are at least three possible sources, namely uncertainties about the inlet conditions in the plane of the valve orifice, 'truncation' errors associated with the finite-difference technique, and possible inadequacies of the turbulence model employed. The second-mentioned source may in principle be eliminated by employing sufficiently fine grid intervals and time steps in the calculations, but economic considerations (i.e. computer costs) place a limit on the degree to which this may be done.

Current efforts are being devoted to improving the accuracy of the numerical method so that this source of error may be better quantified and, hopefully, removed. The improved procedure will then be applied again to the cases just described, as well as to the more recent measurements presented in Section 2.1. Such developments, taken in conjunction with more detailed probing of the inlet region in the experiments, should eventually allow proper assessment and improvement of the remaining source of uncertainty, namely the turbulence model.

Conclusions

The conclusions about the effects of swirl and piston bowl configuration in the non-compressing engine were reported in references 2, 3 and 5. The influence of the piston bowl was shown to be very small compared to that of the simulated valve geometry, unless the bowl is shaped to create and hold a vortex. The addition of swirl vanes upstream of the valve port, inclined at 15° and 30° to the cylinder axis, resulted in elongation of the main vortex, reaching closer to the piston face. Dependent on the level of swirl, new vortices were formed during the intake stroke in the corner between the piston face and the wall and in the near-axis region behind the valve and recirculated a small fraction of the total net mass flowrate.

The more recent results described in the present report, show that the influence of stroke on the flow patterns can be considered of minor importance. In the first part of the intake process the higher momentum of the jet, in the case of the longer stroke, causes the formation of stronger vortices with consequent suppression of the small vortex between the cylinder head and the axis, observed with the shorter stroke. At mid-stroke, the flow patterns are almost identical with vortices of equal strength. As the piston approaches BDC the influence of the longer stroke is to weaken the main and corner vortices thus causing their earlier destruction at the beginning of the exhaust stroke.

Similar conclusions can be drawn for the influence of the clearance volume on the flow patterns. At the early part of the intake stroke smaller clearance causes stronger impingement of the jet on the piston generating higher turbulence near to it; the created vortices are just stronger than the corresponding ones with the 30mm clearance and occupy most of the flow space. The stronger main vortex at midstroke breaks up creating a small vortex near the axis just before the piston reaches BDC. The system of vortices is also destroyed at the beginning of the exhaust stroke resulting in similar flow patterns to the ones of the larger clearance at 190° and 200° . Overall, the influence of stroke and clearance on the flow patterns is not very significant, with the shorter stroke and smaller clearance cases being slightly more "attractive" from the turbulence point of view.

Measurements of swirl velocity with compression at 675 rpm show close correspondence with the non-compressing results (500 rpm) on the intake stroke and on the compression stroke, until the inlet valve closes. At this point the compressing flow tends towards solid body rotation whereas the velocity maximum in the non-compressing flow moves from the near wall to the central region of the cylinder.

Concerning the predictions, the comparisons reveal that the RPM method is capable of reproducing the major features of the in-cylinder motion in the non-compressing engine, as influenced by inlet swirl and piston geometry. However, the quantitative agreement in respect of both mean velocity and turbulence intensity is sometimes poor, for reasons which have yet to be precisely identified, but are believed to be due to one or more of the following factors: uncertainties in inlet conditions and inaccuracies in the finite-difference procedure and/or turbulence model.

References

1. A.D. Gosman, A. Melling, A.P. Watkins and J.H. Whitelaw, (1978). Axisymmetric flow in a motored reciprocating engine. Proc. Inst. Mech. Eng. 192, 213
2. A.P. Morse, J.H. Whitelaw and M. Yianneskis (1979). Turbulent flow measurements by laser-Doppler anemometry in a motored piston/cylinder assembly. J. Fluids Eng. 101, 208.
3. A.P. Morse, J.H. Whitelaw and M. Yianneskis (1979). The influence of swirl on the flow characteristics of a reciprocating piston-cylinder assembly. AERE, Harwell Report R9510. To be published in J. Fluids Eng.
4. A.P. Morse, J.H. Whitelaw and M. Yianneskis (1979). Influence of speed on the flow patterns in motored reciprocating engines. Imperial College, Mech. Eng. Dept. Report FS/79/12.
5. A.F.Bicen, N. Vlachos and J.H. Whitelaw (1980). The creation and destruction of vortices in unsteady flows. Letters in Heat and Mass Transfer. 7, 77.
6. A.P. Morse, J.H. Whitelaw and M. Yianneskis (1979). The flow characteristics of a piston-cylinder assembly with an off-centre, open port. Imperial College, Mech. Eng. Dept. Report FS/79/11. To be published in J. Mech. Eng. Sci.
7. P. Hutchinson, A.P. Morse and J.H. Whitelaw (1978). Velocity measurements in motored engines: experience and prognosis. SAE Paper 780061.
8. A.D. Gosman and J.H. Whitelaw (1980). Calculation and measurement of flow and heat transfer properties of reciprocating, piston-cylinder arrangements. Proc. SRC/UNICEG Symposium, 131.
9. A. Melling and J.H. Whitelaw (1976). Design of laser-Doppler anemometers for reciprocating engines. Imperial College, Mech. Eng. Dept. Report CHT/76/6.
10. A.P. Morse (1980) Laser-Doppler measurements of the in-cylinder flow in a motored four-stroke reciprocating engine. Imperial College, Mech. Eng. Dept. Report FS/80/ 27.

11. A.D. Gosman and A.P. Watkins, (1977). A computer prediction method for turbulent flow and heat transfer in piston/cylinder assemblies. Presented at Symposium on Turbulent Shear Flows, Pennsylvania State University, April 18-20, 1977. Also Imperial College, Mech. Eng. Dept. Report FS/77/10.
12. A.D. Gosman, R.J.R. Johns and A.P. Watkins, (1978). Assessment of a prediction method for in-cylinder processes in reciprocating engines. Proc. General Motors Symposium on Combustion Modelling in Reciprocating Engines, Detroit, Nov. 6-7.
13. W.C. Reynolds (1978). Modelling of fluid motions in engines; an introductory overview. Proc. General Motors Symp. on Combustion Modelling in Reciprocating Engines, Detroit, Nov. 6-7.
14. F.C. Lockwood (1977). The modelling of premixed and diffusion turbulent combustion. Combustion and Flame, 29, no.2.
15. A.D. Gosman and R.J.R. Johns (1979). Computer analysis of fuel-air mixing in direct-injection engines. Imperial College Mech. Eng. Dept., Report FS/79/20.
16. A.D. Gosman and R.J.R. Johns, (1978). Development of a predictive tool for in-cylinder gas motion in engines. SAE 780315.
17. A.F. Bicen and N.S. Vlachos (1980). Influence of stroke and clearance on the flow patterns in motored piston-cylinder assemblies. Imperial College Mech. Eng. Dept. Report FS/80/28.

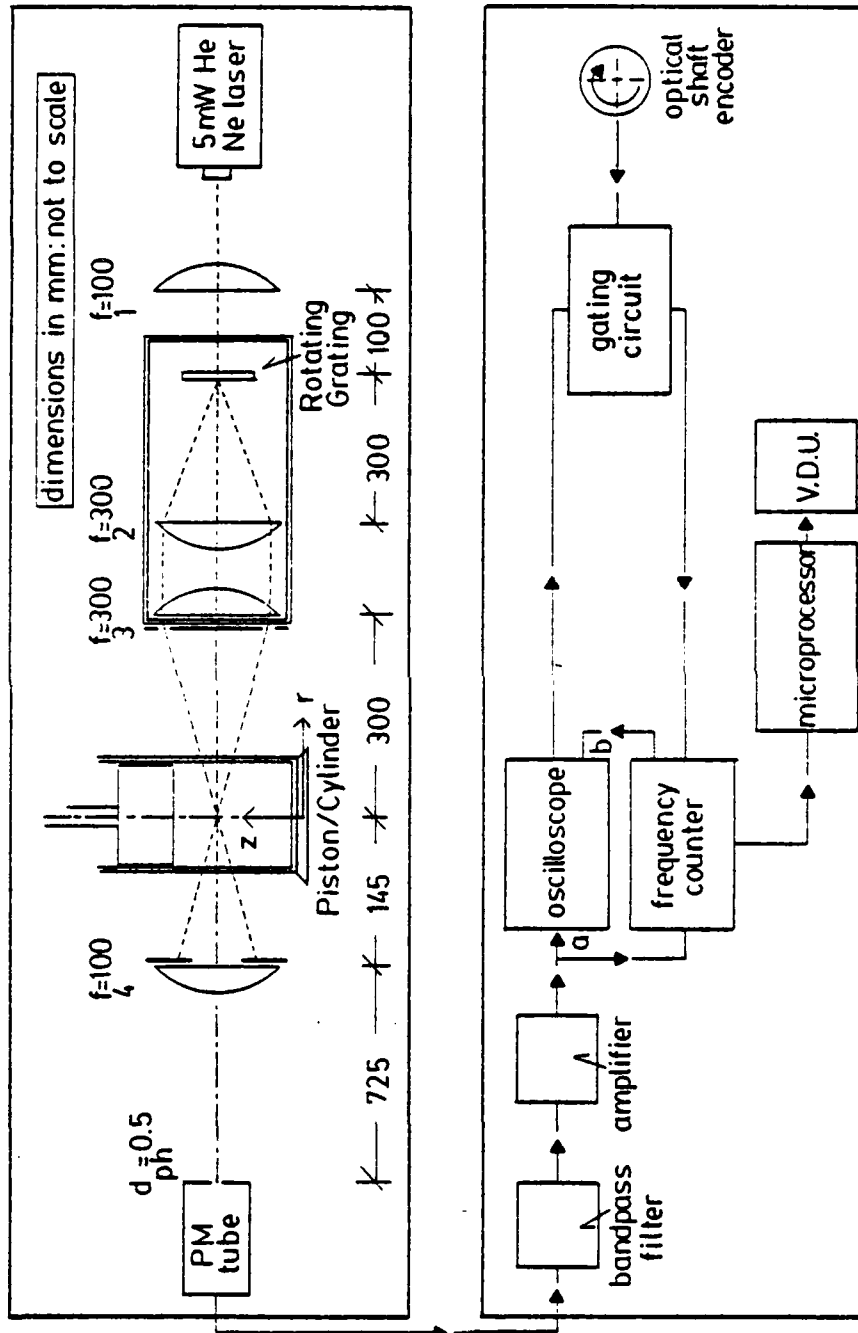


Figure 1. Block diagram of optical and signal processing arrangements.

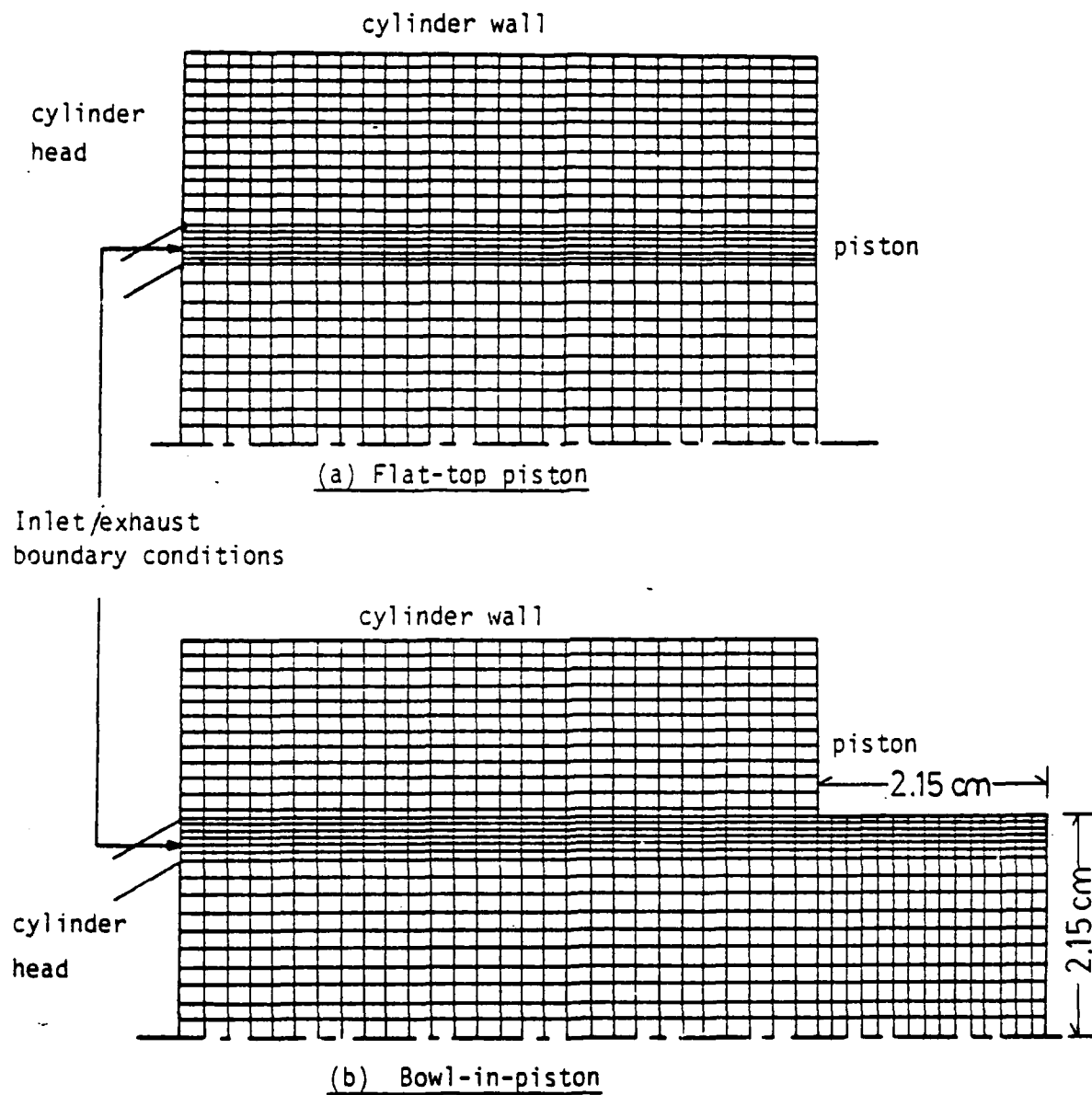


Fig. 2 Computational grids used for the simulation of the
experiments of Morse et al (1978)

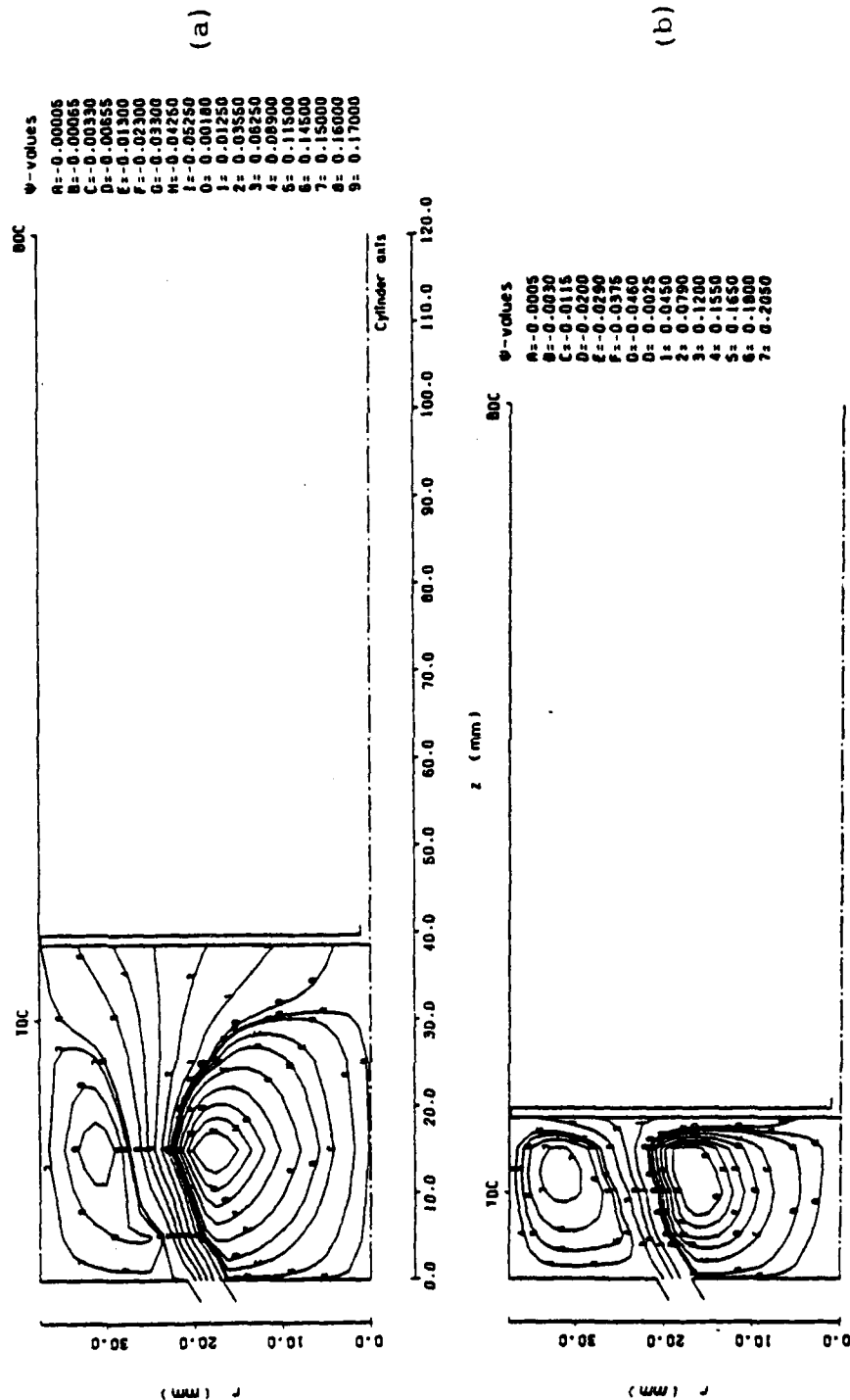


Figure 3. Streamline patterns at 36° Crank angle
 (a) Stroke of 90mm, Clearance of 30mm
 (b) Stroke of 90mm, Clearance of 10mm

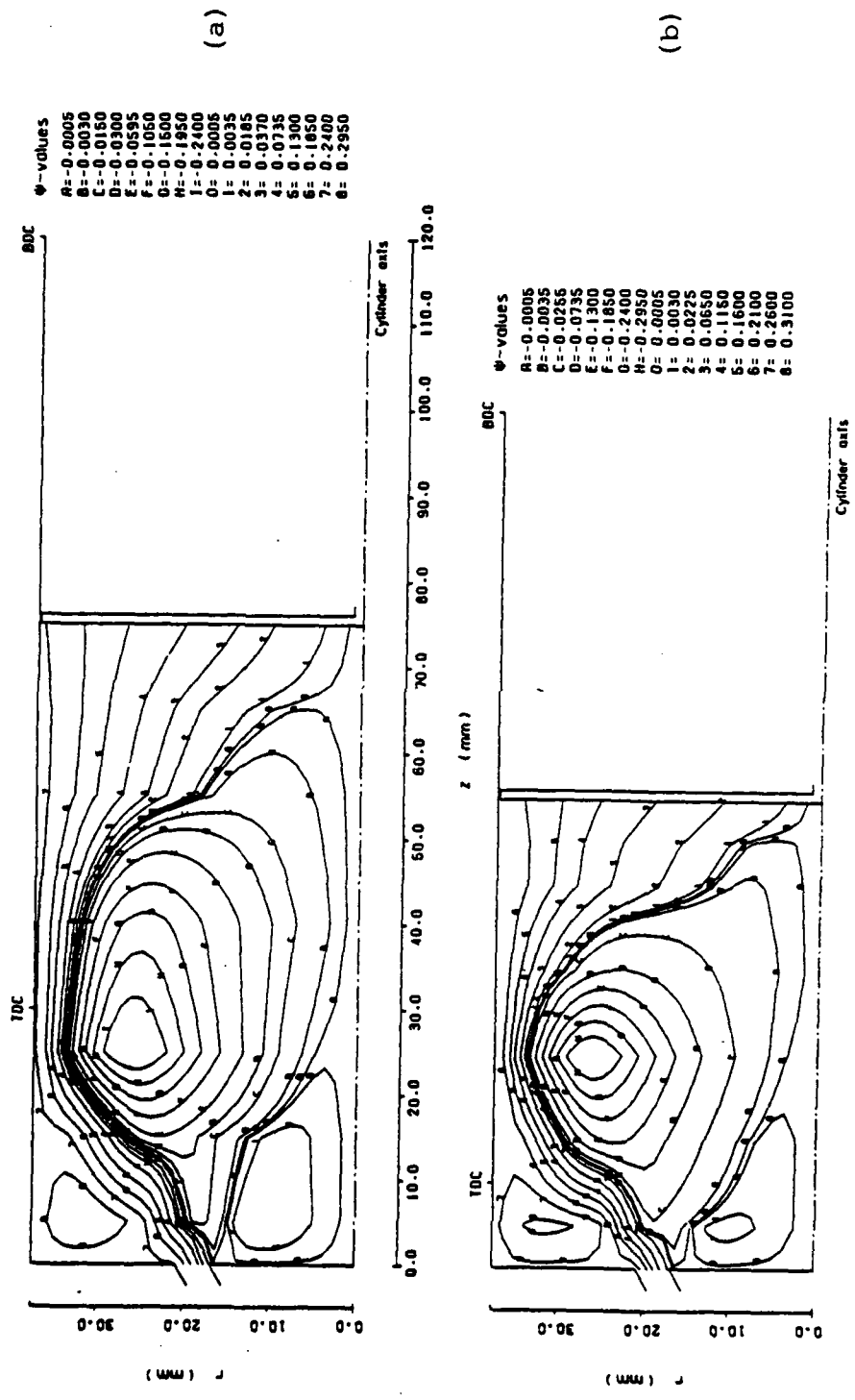


Figure 4. Streamline patterns at 90° Crank angle
 (a) Stroke of 90mm, Clearance of 30mm
 (b) Stroke of 90mm, Clearance of 10mm

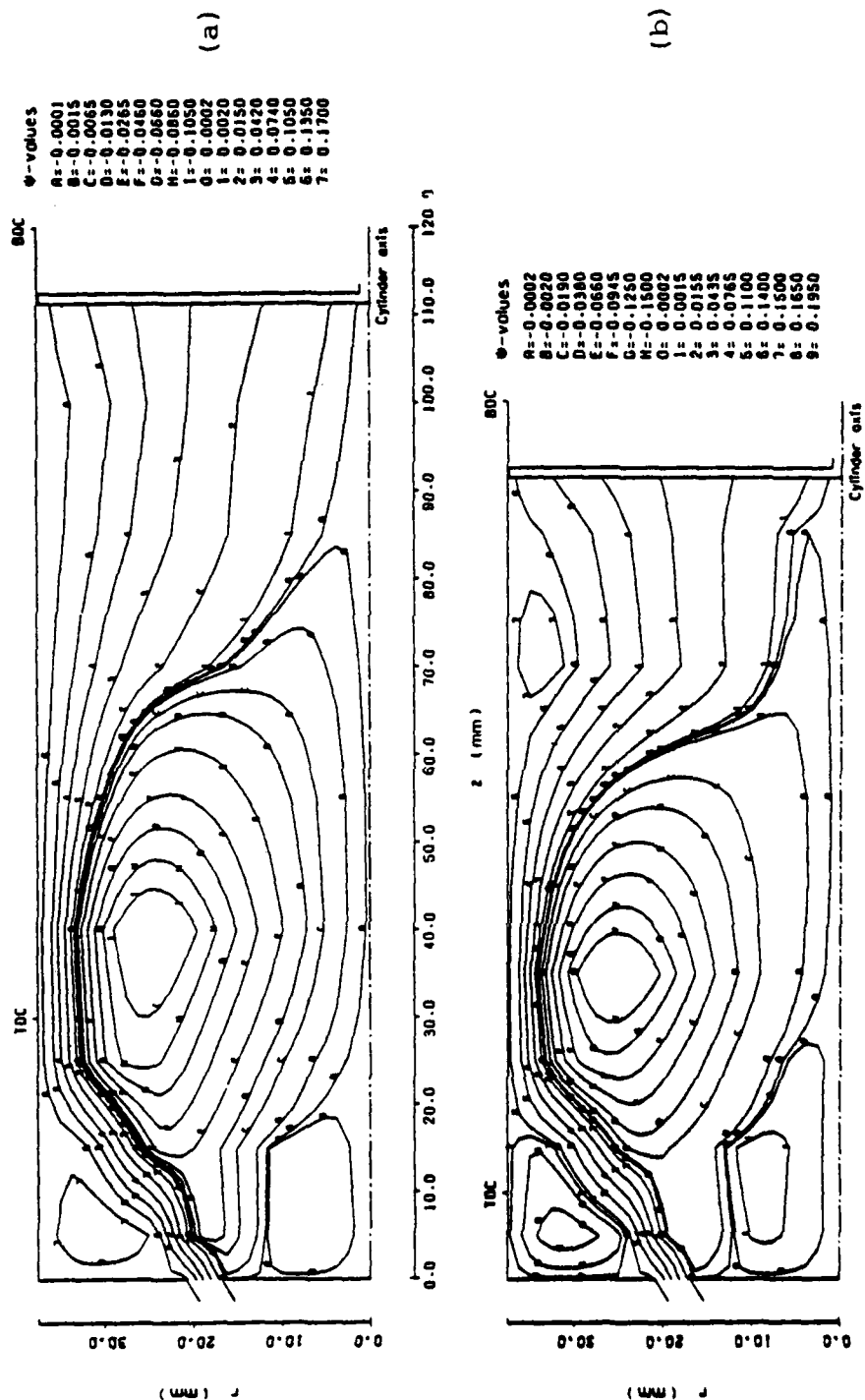


Figure 5. Streamline patterns at 144° Crank angle
 (a) Stroke of 90mm, Clearance of 30mm
 (b) Stroke of 90mm, Clearance of 10mm

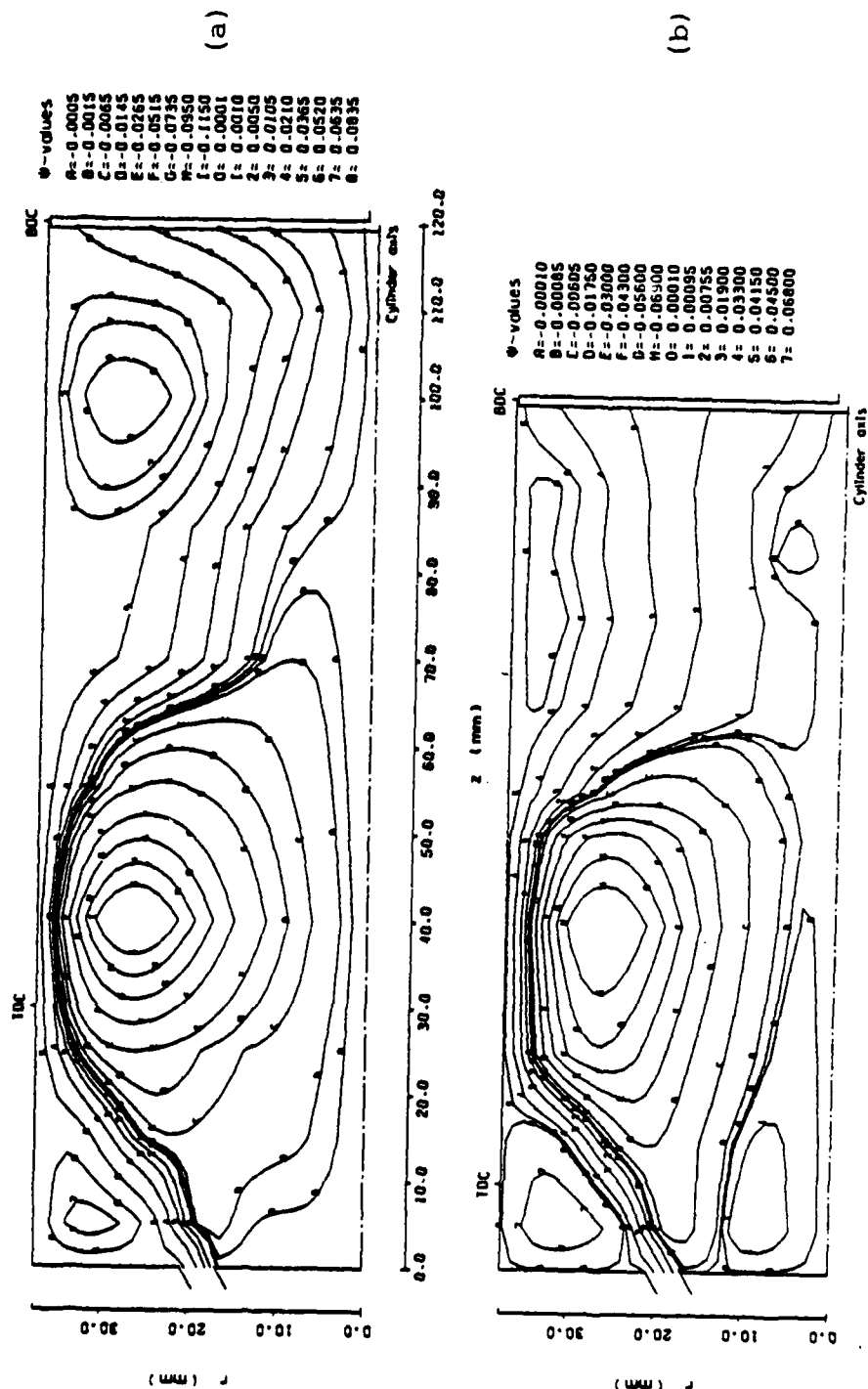


Figure 6. Streamline patterns at 170° Crank angle
 (a) Stroke of 90mm, Clearance of 30mm
 (b) Stroke of 90mm, Clearance of 10mm

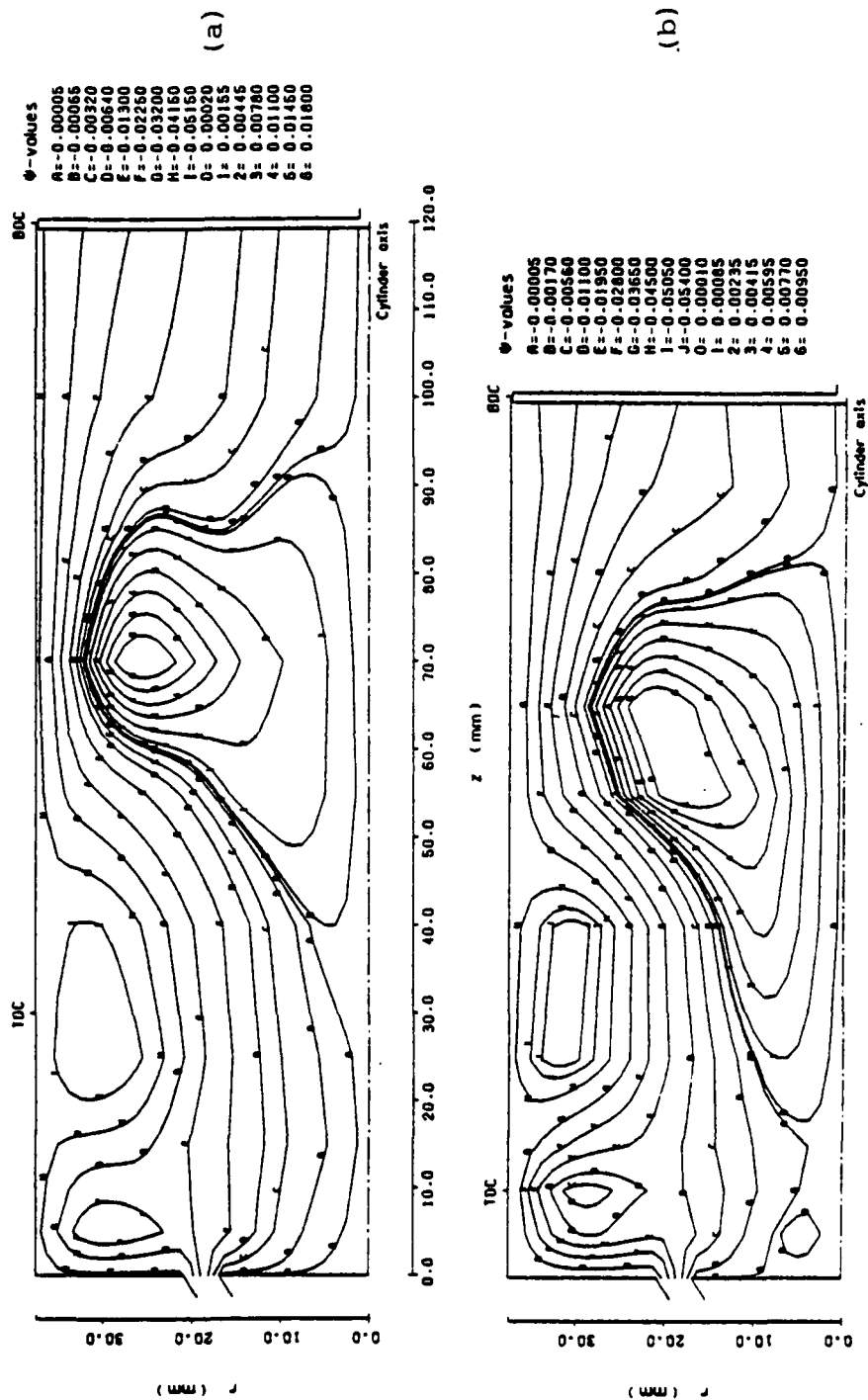


Figure 7. Streamline patterns at 190° Crank angle
 (a) Stroke of 90mm, Clearance of 30mm
 (b) Stroke of 90mm, Clearance of 10mm

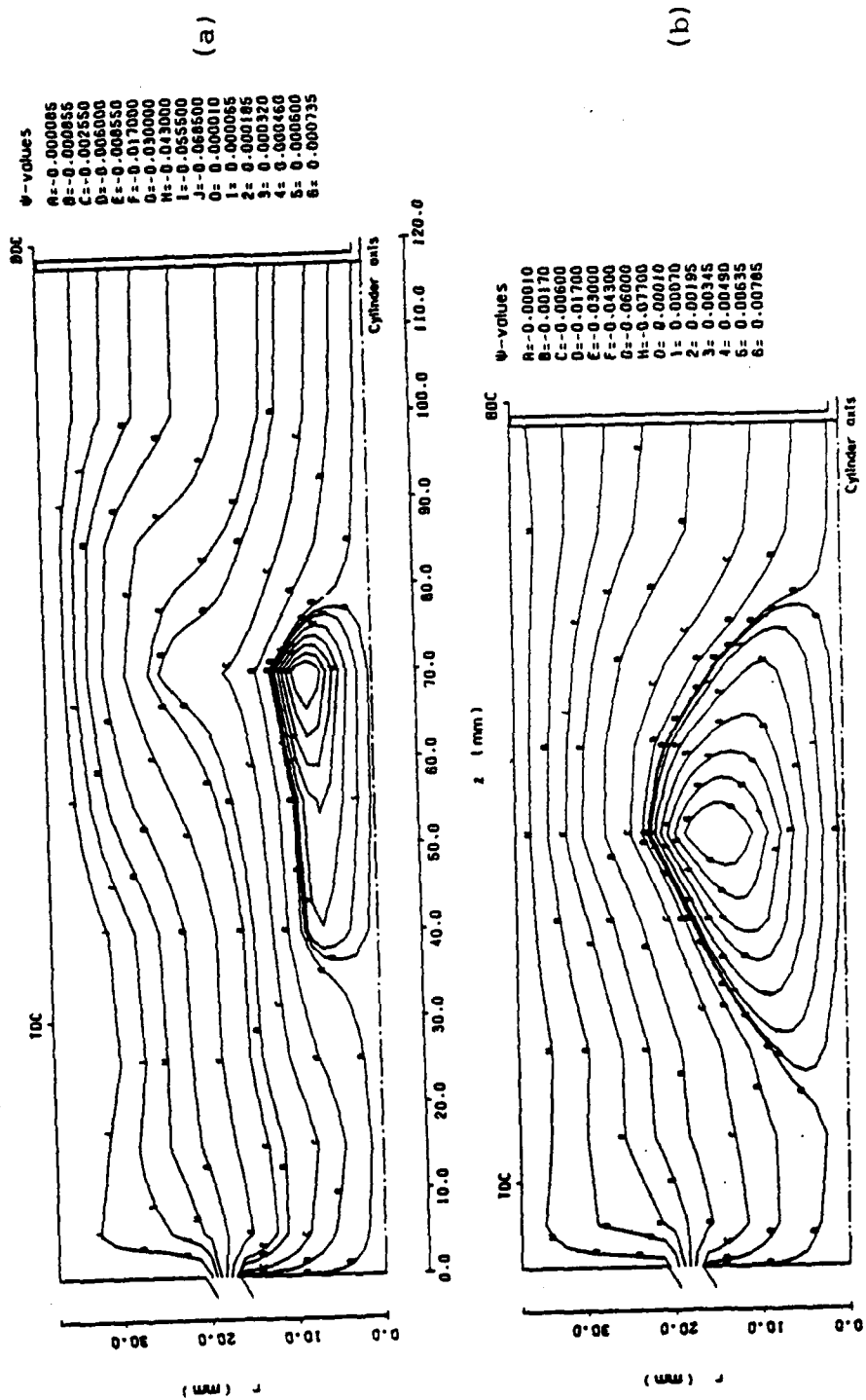


Figure 8. Streamline patterns at 200° crank angle
 (a) Stroke of 90mm, Clearance of 30mm
 (b) Stroke of 90mm, Clearance of 10mm

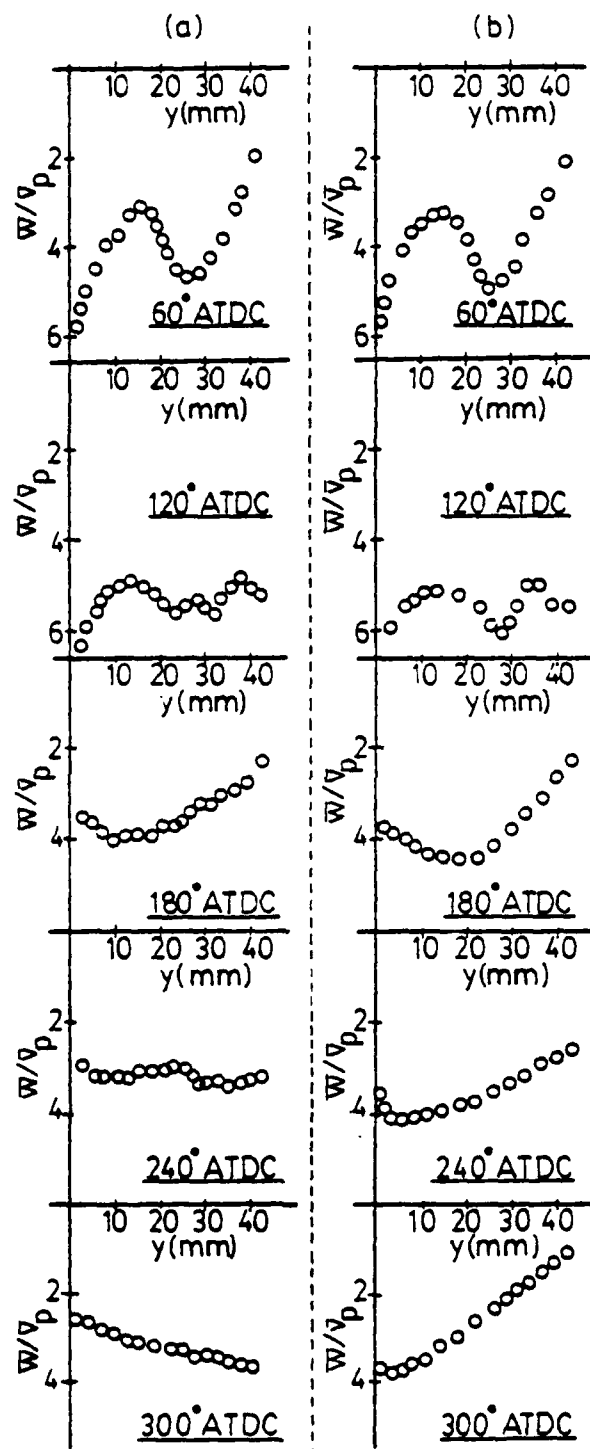


Figure 9. (a) Without compression ($z=10\text{mm}$, 500rpm)
 (b) With compression ($z=10\text{mm}$, 675rpm)

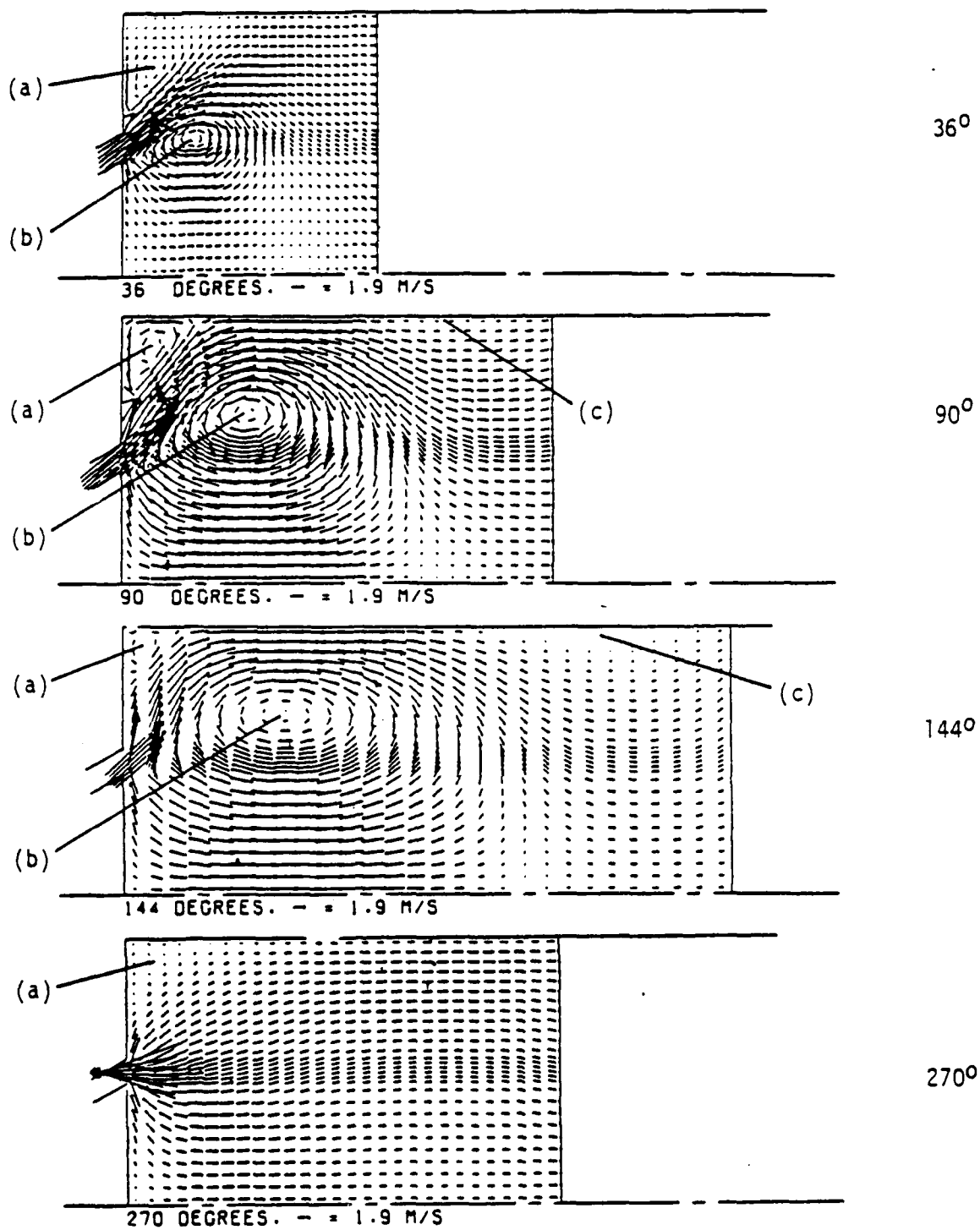
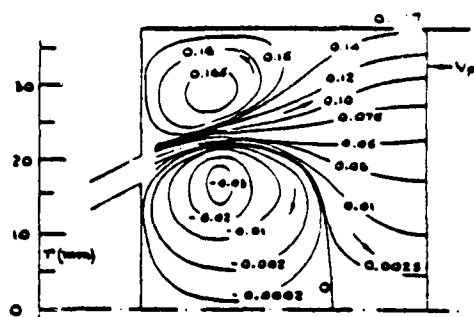
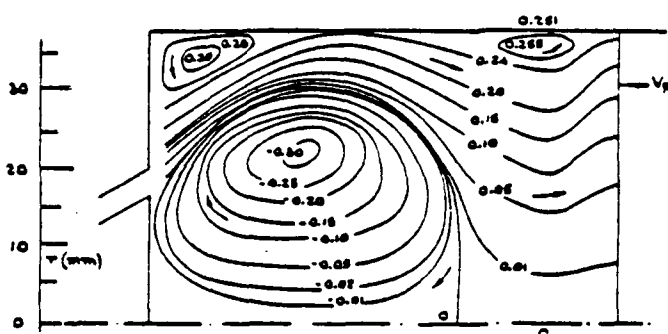


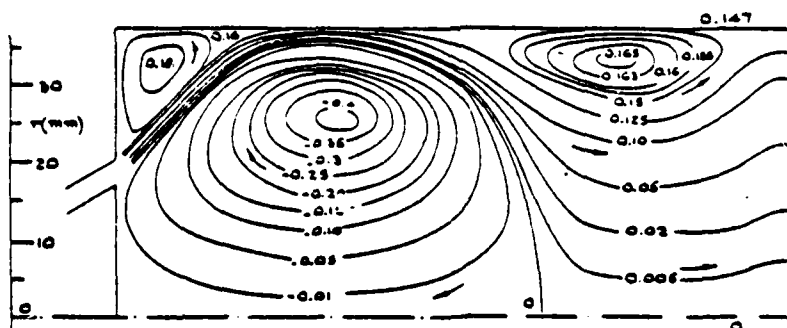
Fig. 10 Predicted axial-radial velocity fields for case 1



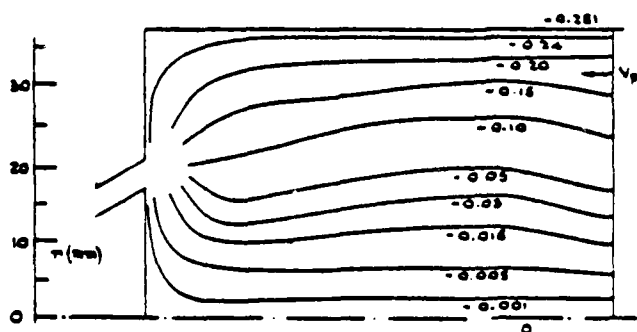
36°



90°



144°



270°

0 10 20 30 40 50 60 70 80
z (mm)

Fig. 11 Streamlines for the experiments, without swirl,
of Morse et al (1978)

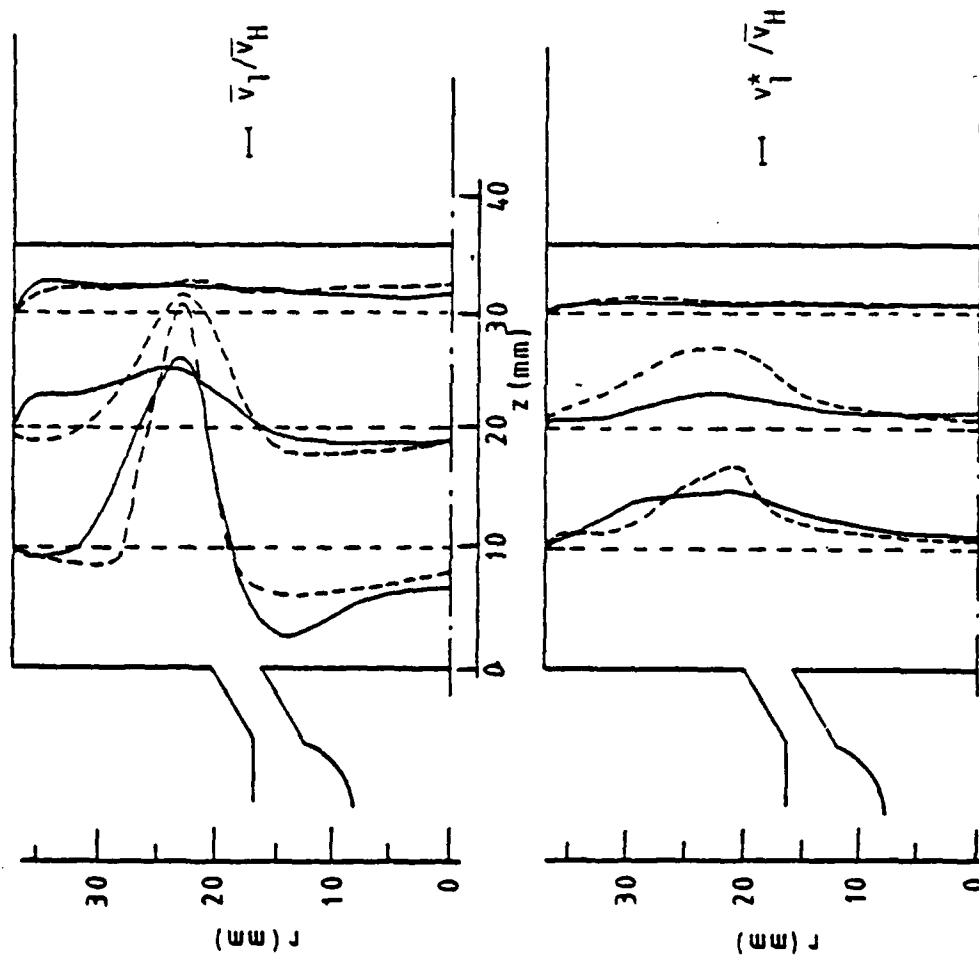


Fig. 12 Measured (---) and calculated (—) mean and turbulent axial velocities at 36° for case 1

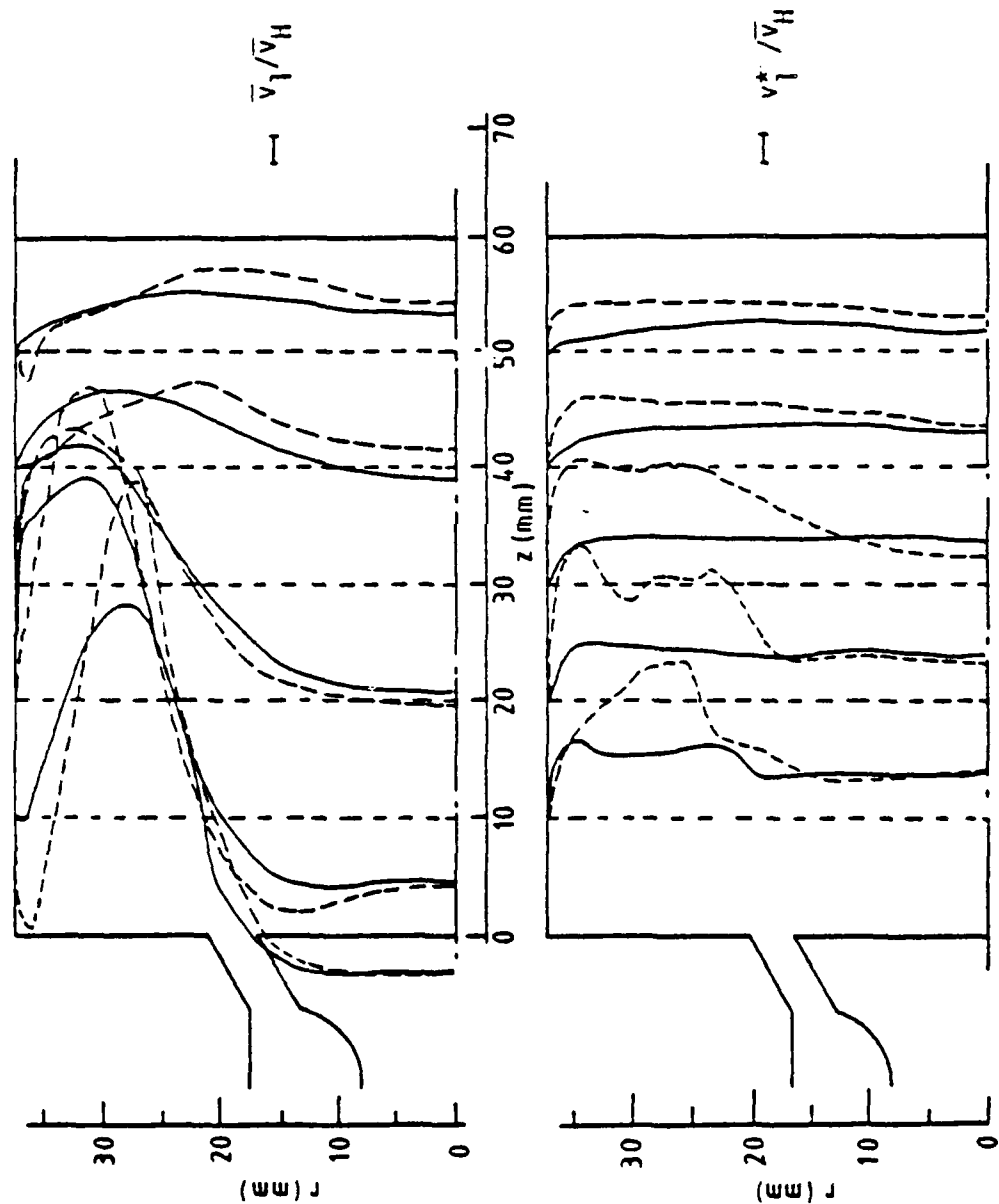


Fig. 13 Measured (---) and calculated (—) mean and turbulent axial velocities at 90° for case 1

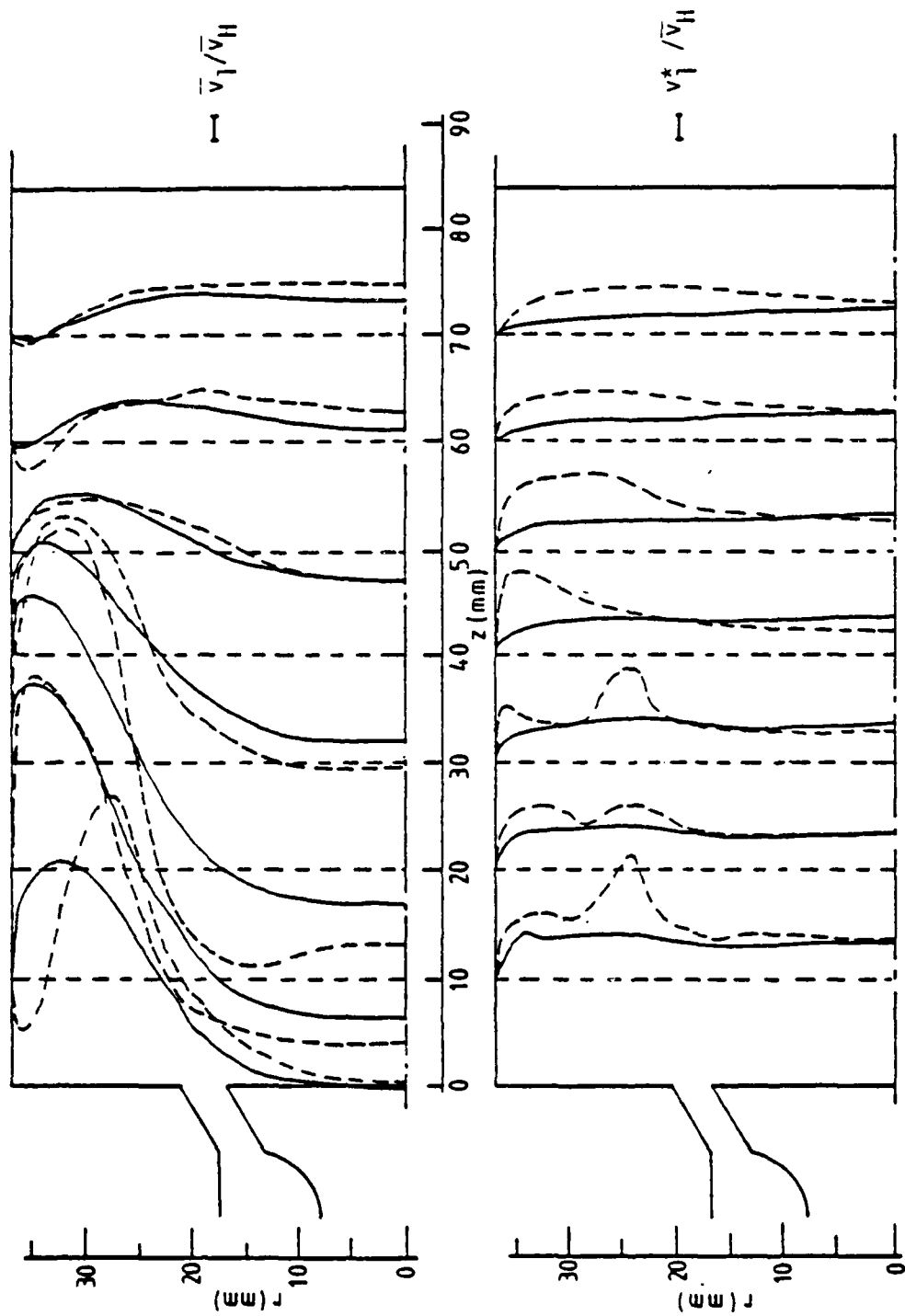


Fig. 14 Measured (---) and calculated (—) mean and turbulent axial velocities at 144° for case I

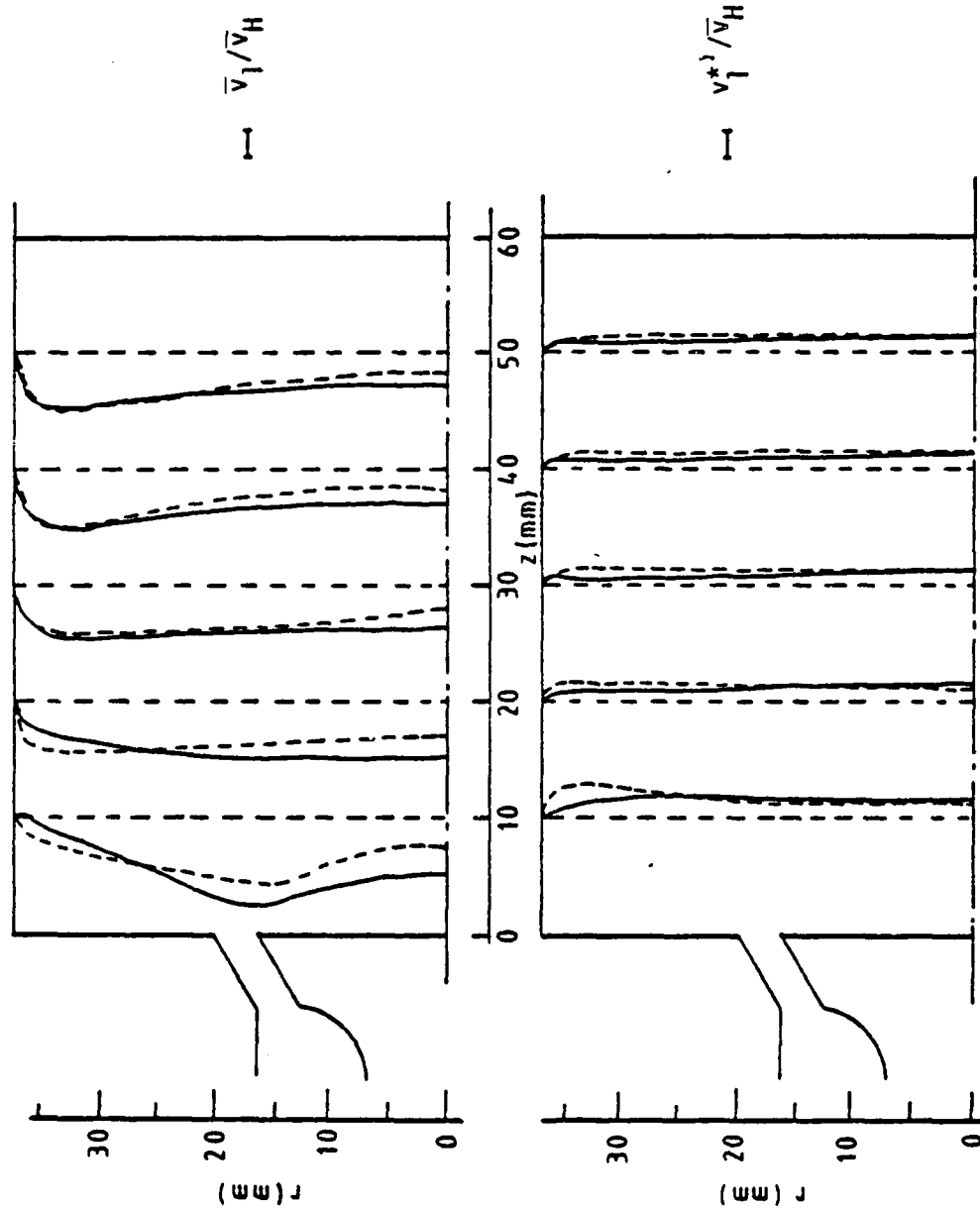


Fig. 15 Measured (---) and calculated (—) mean and turbulent axial velocities at 270° for case 1

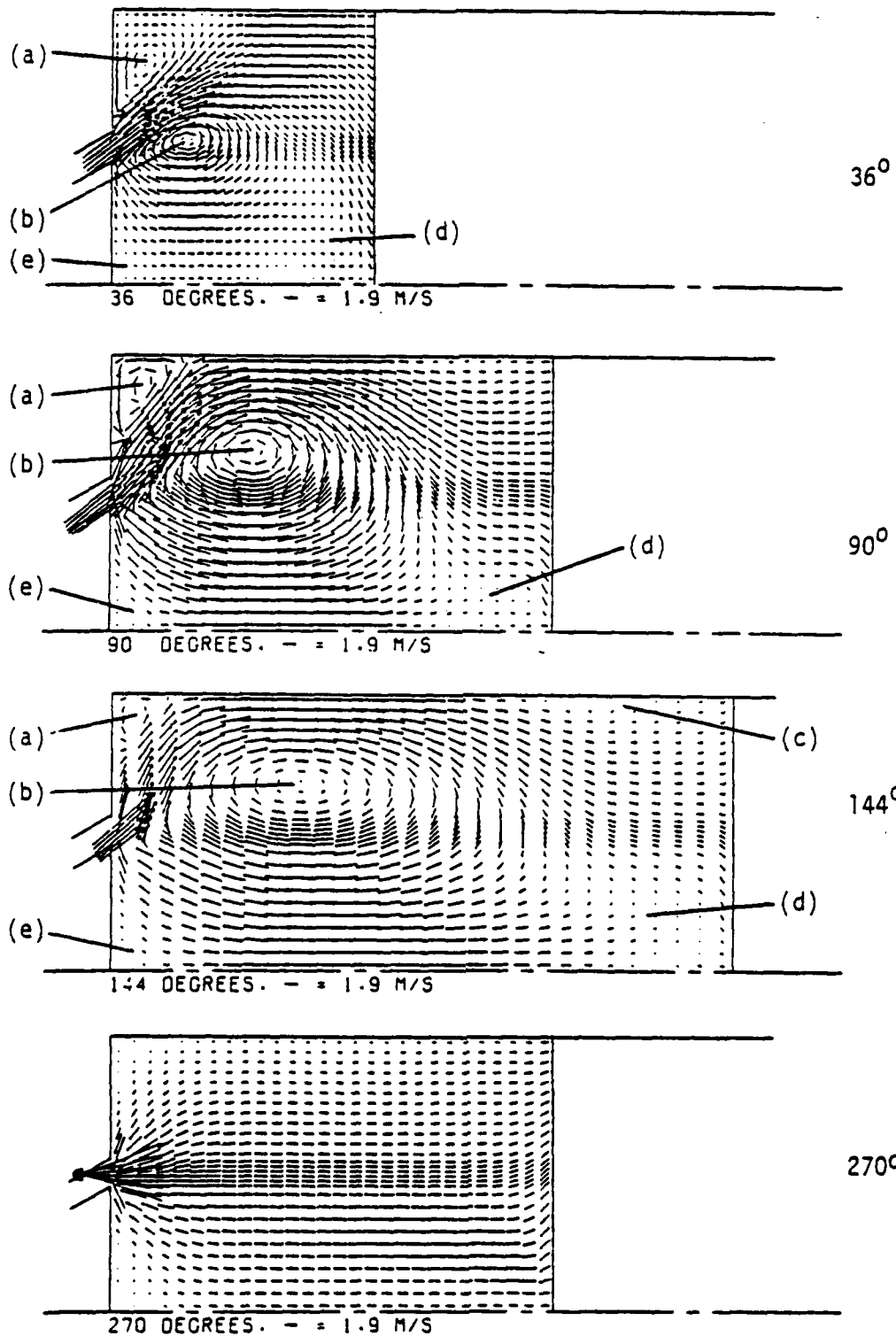
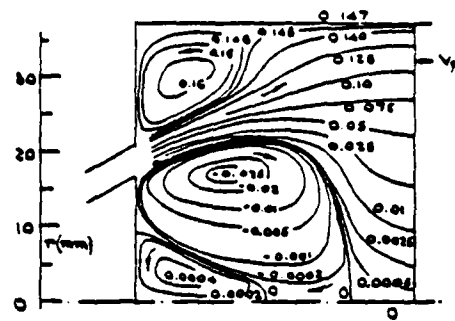
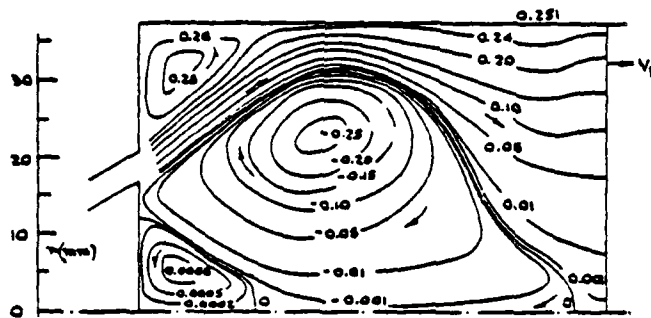


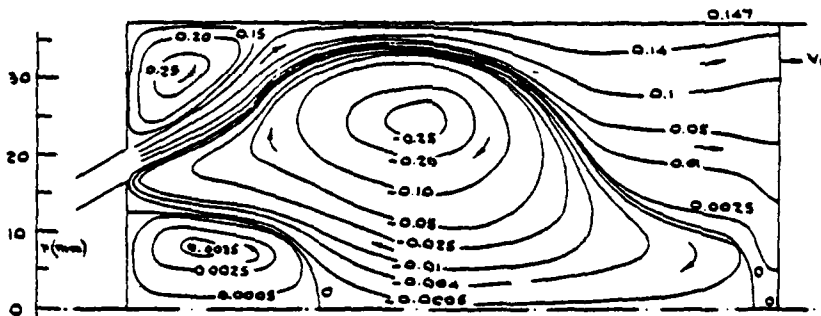
Fig. 16 Predicted axial-radial velocity fields for case 2



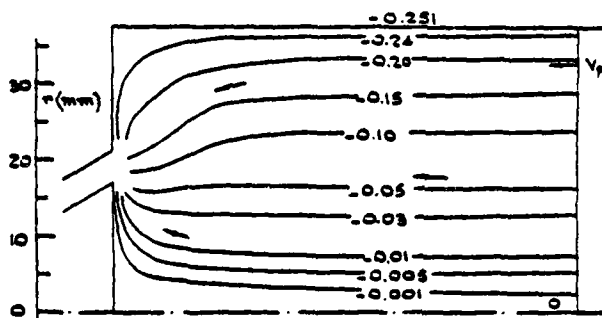
36°



90°



144°



270°

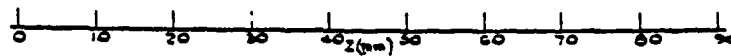


Fig. 17 Streamlines for the experiments, with swirl,
of Morse et al (1978)

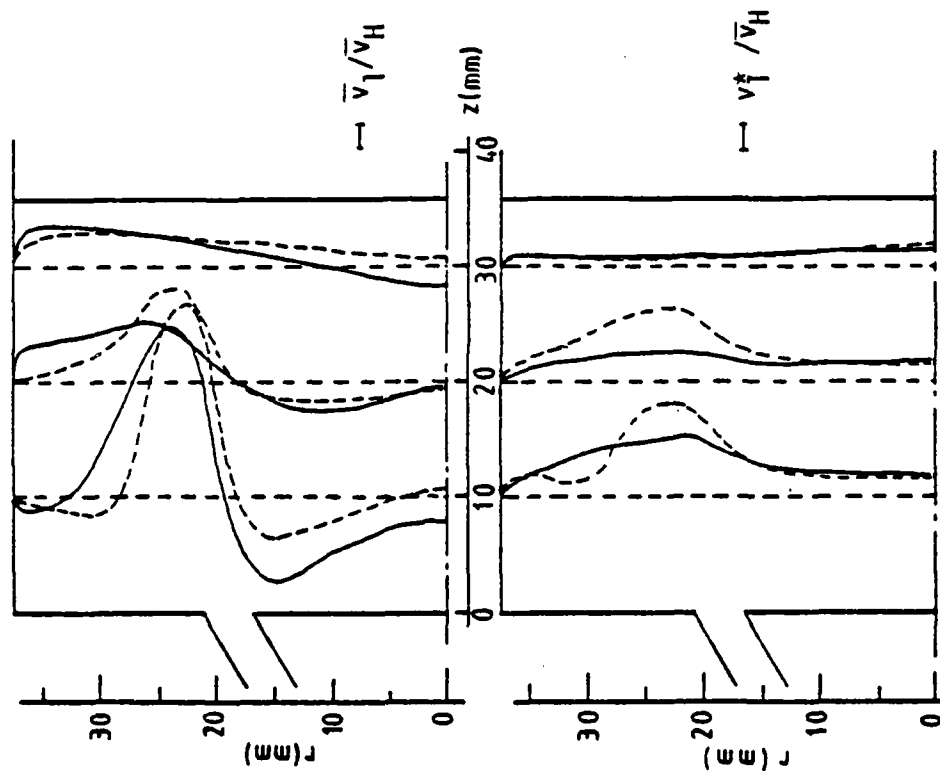


Fig. 18 Measured: (---) and calculated (—) mean and turbulent axial velocities at 36° for case 2

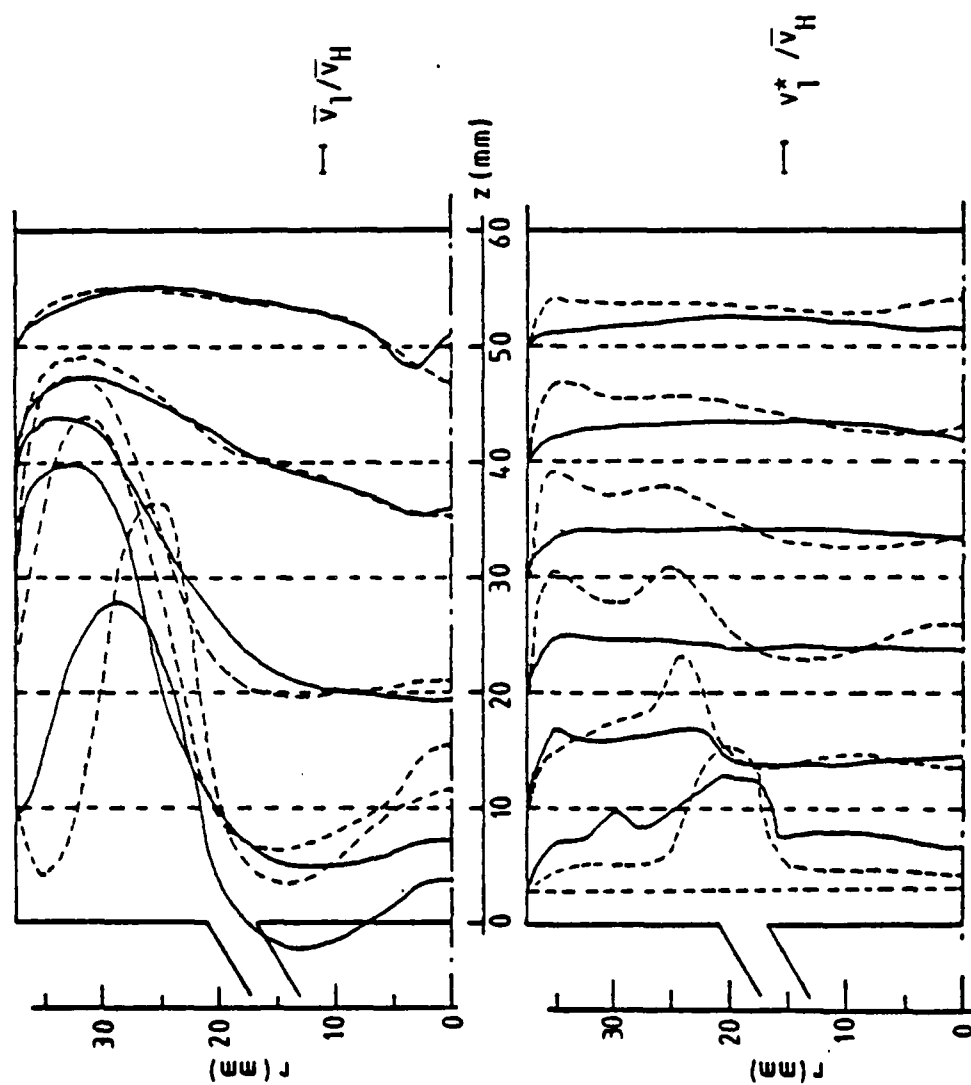


Fig. 19 Measured (---) and calculated (—) mean and turbulent axial velocities

at 90° for case 2

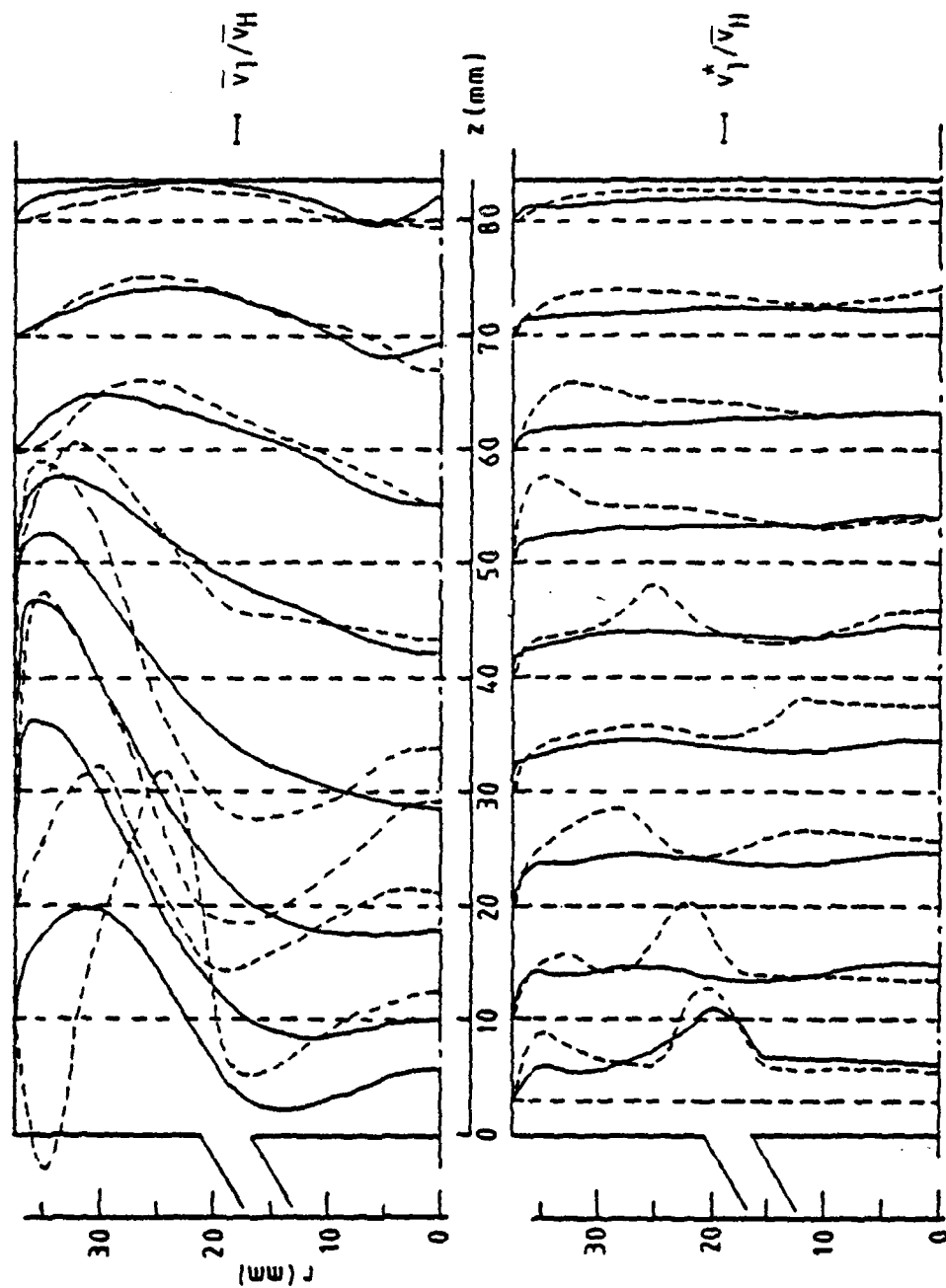


Fig. 20 Measured (---) and calculated (—) mean and turbulent axial velocities at 144° for case 2

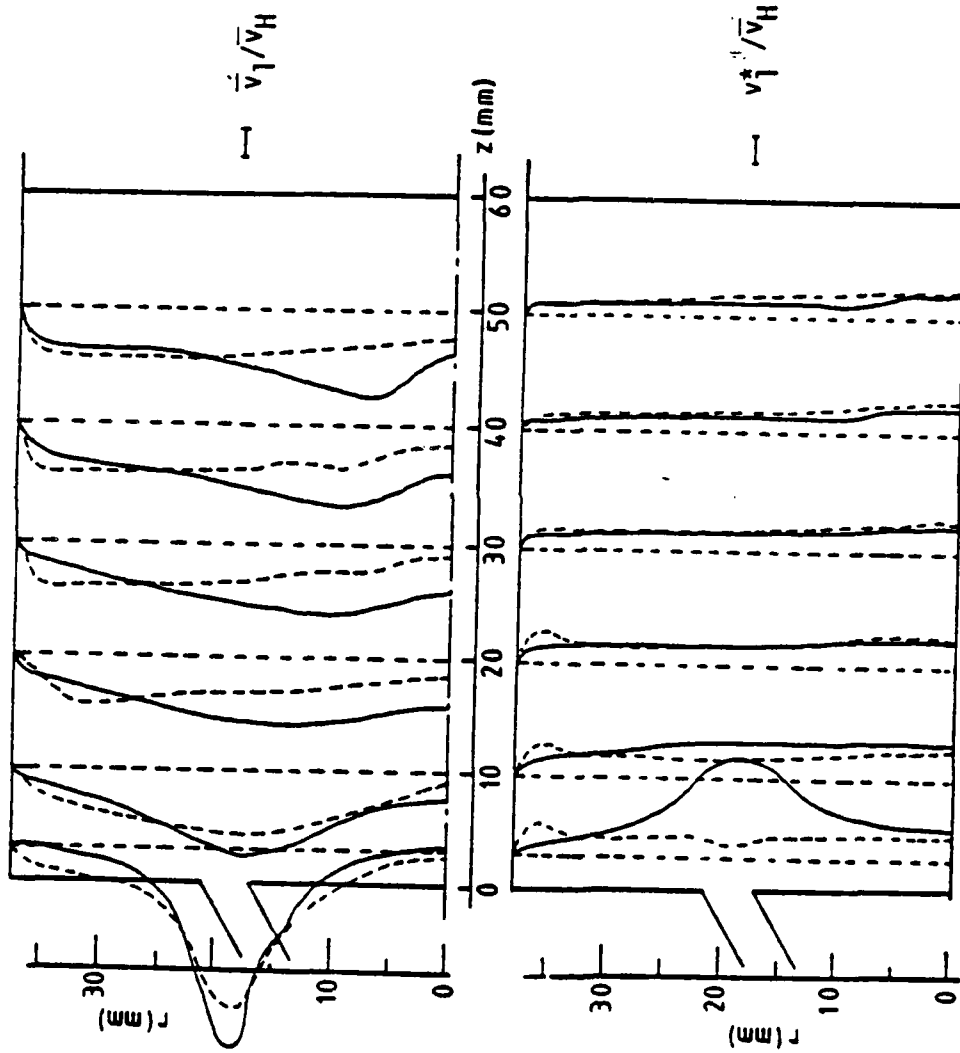


Fig. 21 Measured (---) and calculated (—) mean and turbulent axial velocities at 270° for case 2

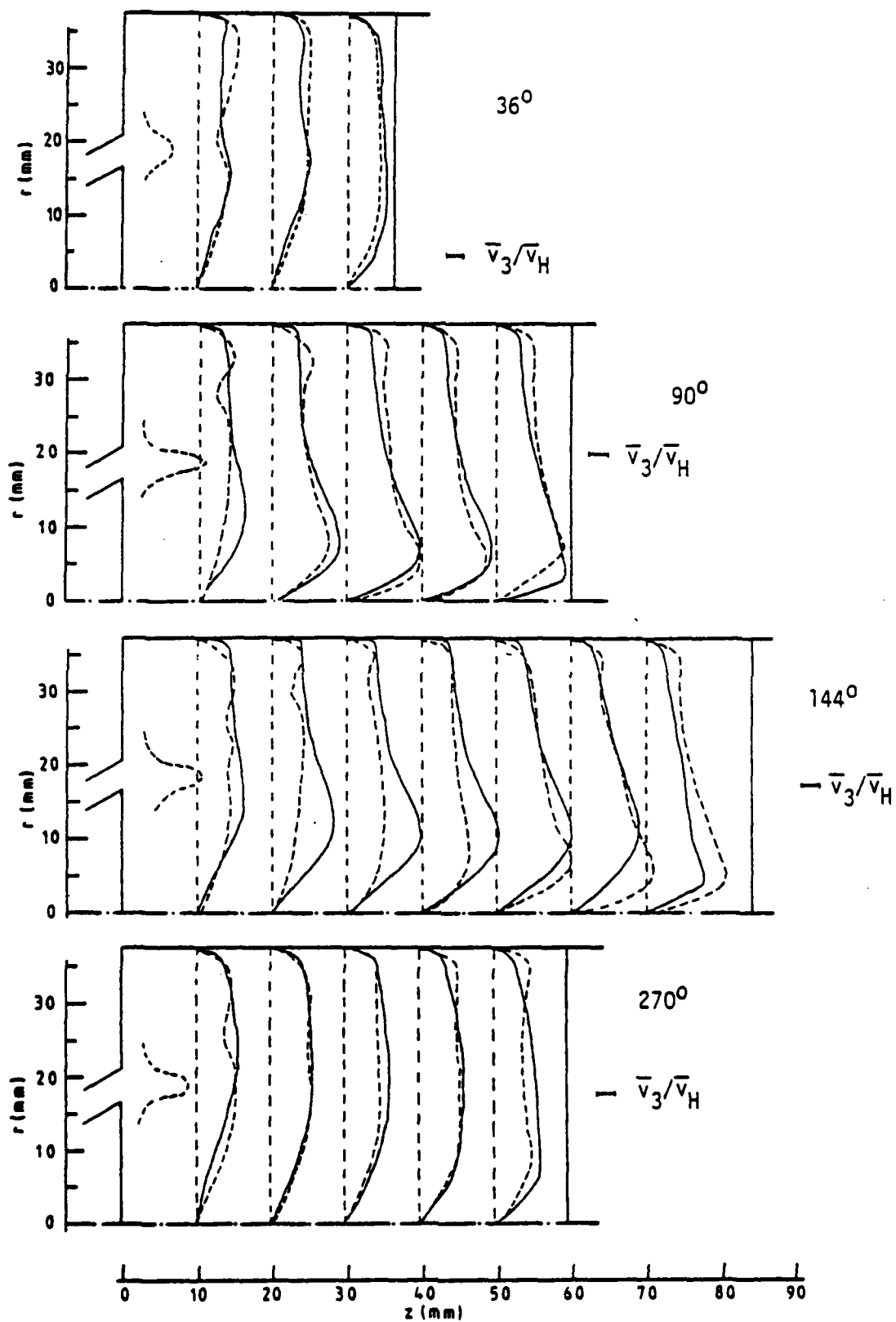


Fig. 22 Measured (---) and calculated (—) swirl
velocities for case 2

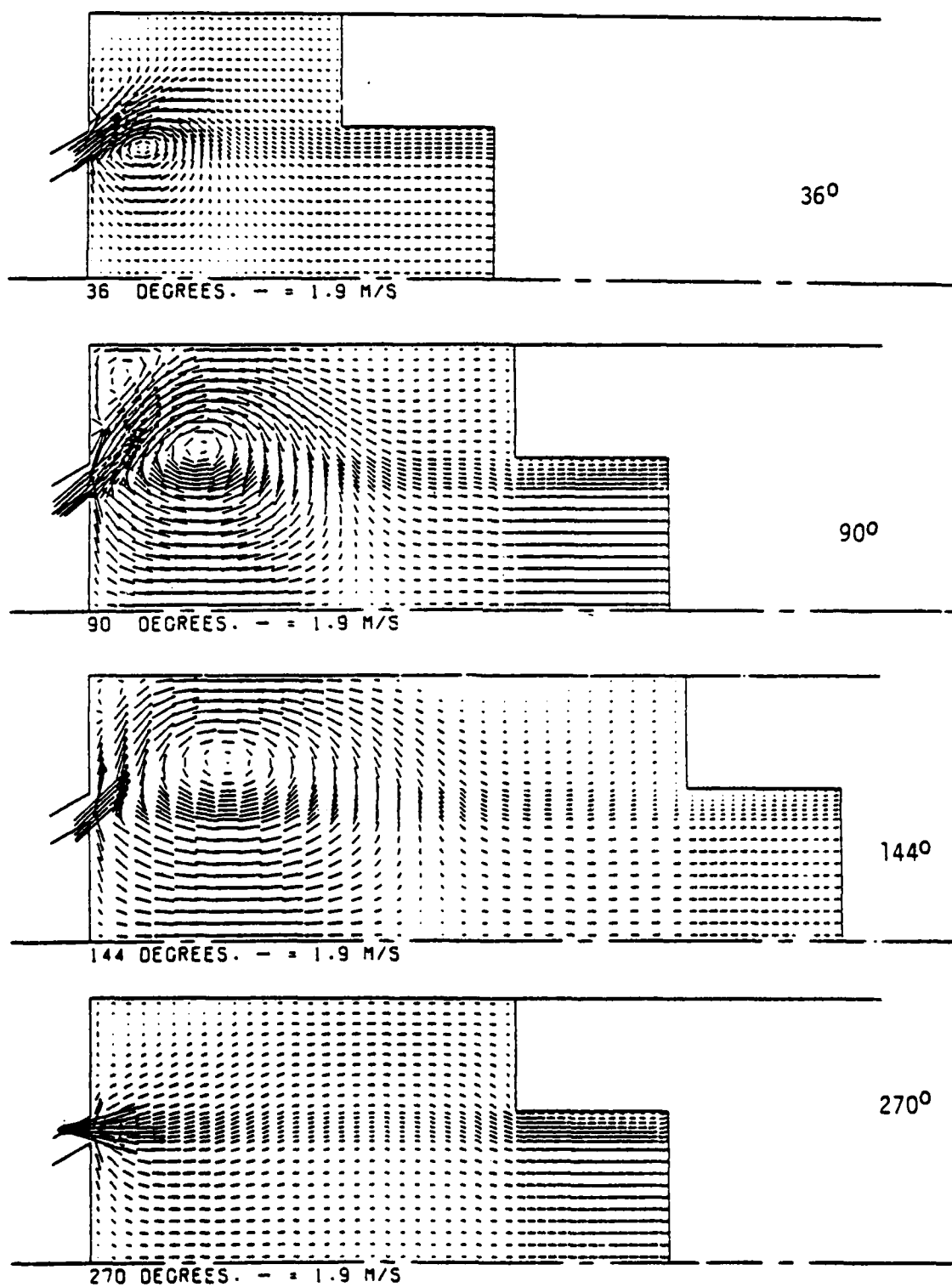


Fig. 23 Predicted axial-radial velocity fields for case 3

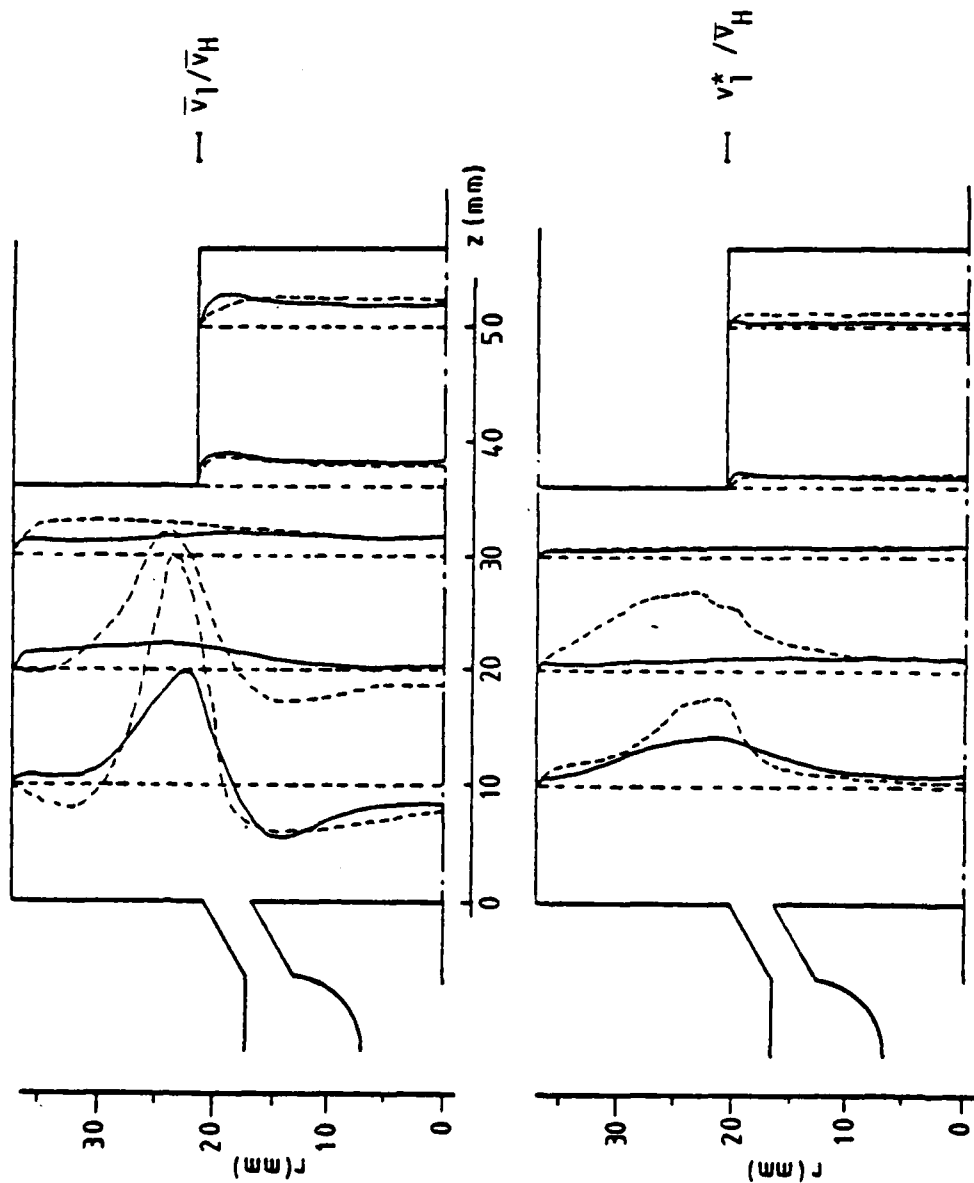


Fig. 24 Measured (---) and calculated (—) mean and turbulent axial velocities at 36° for case 3

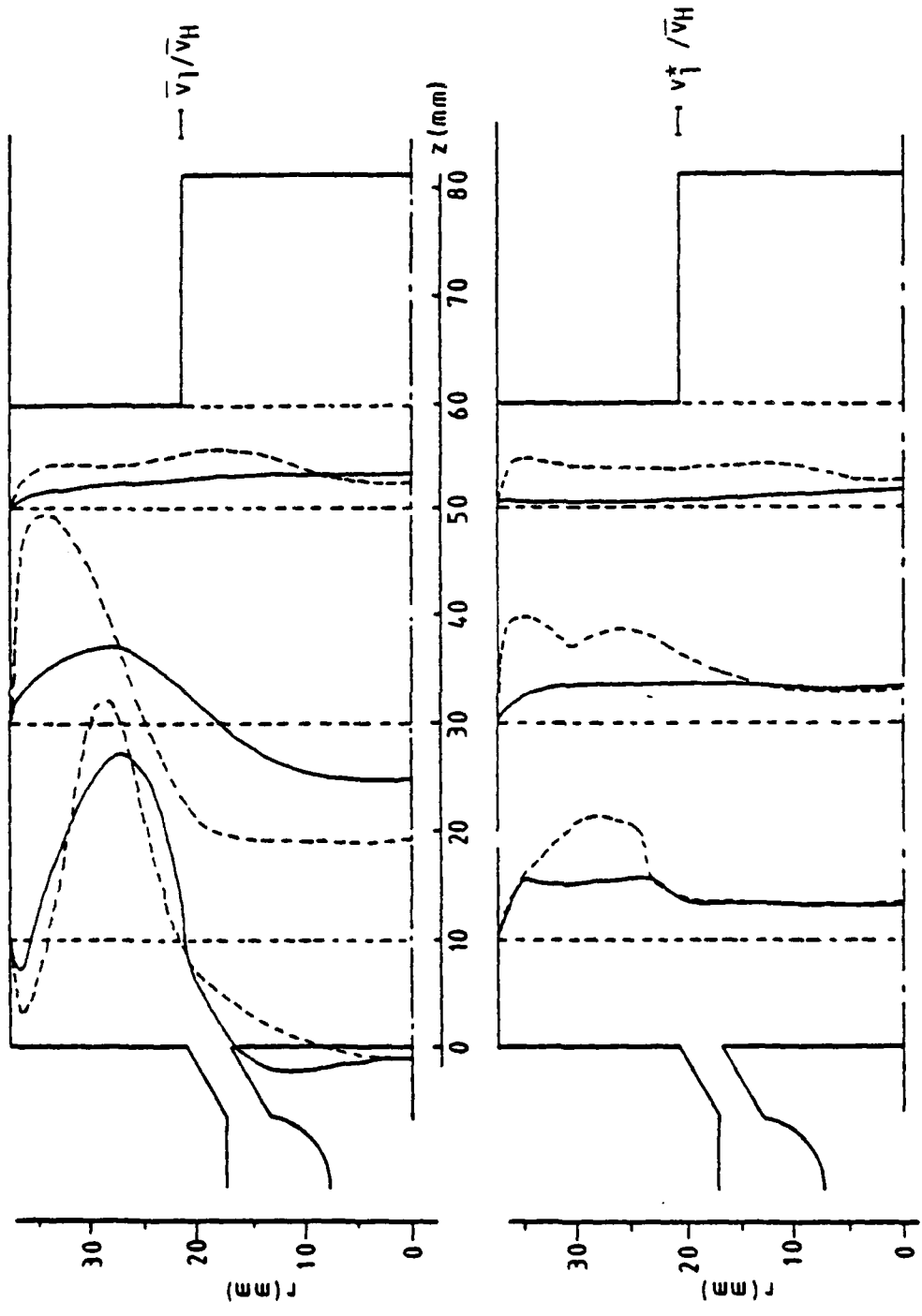


Fig. 25 Measured (---) and calculated (—) mean and turbulent axial velocities
at 90° for case 3

contd....

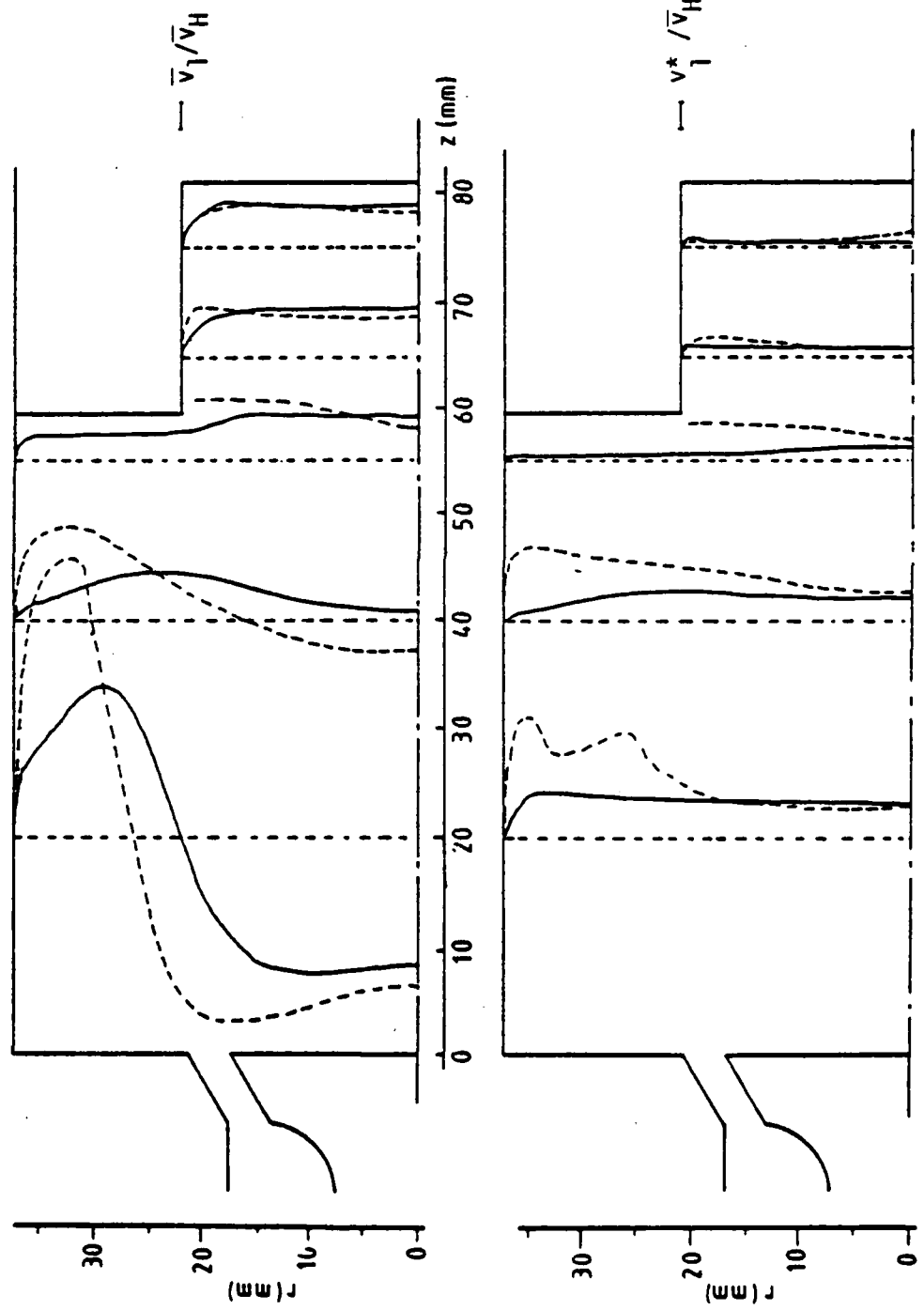


Fig. 25 Measured (---) and calculated (—) mean and turbulent axial velocities at 90° for case 3

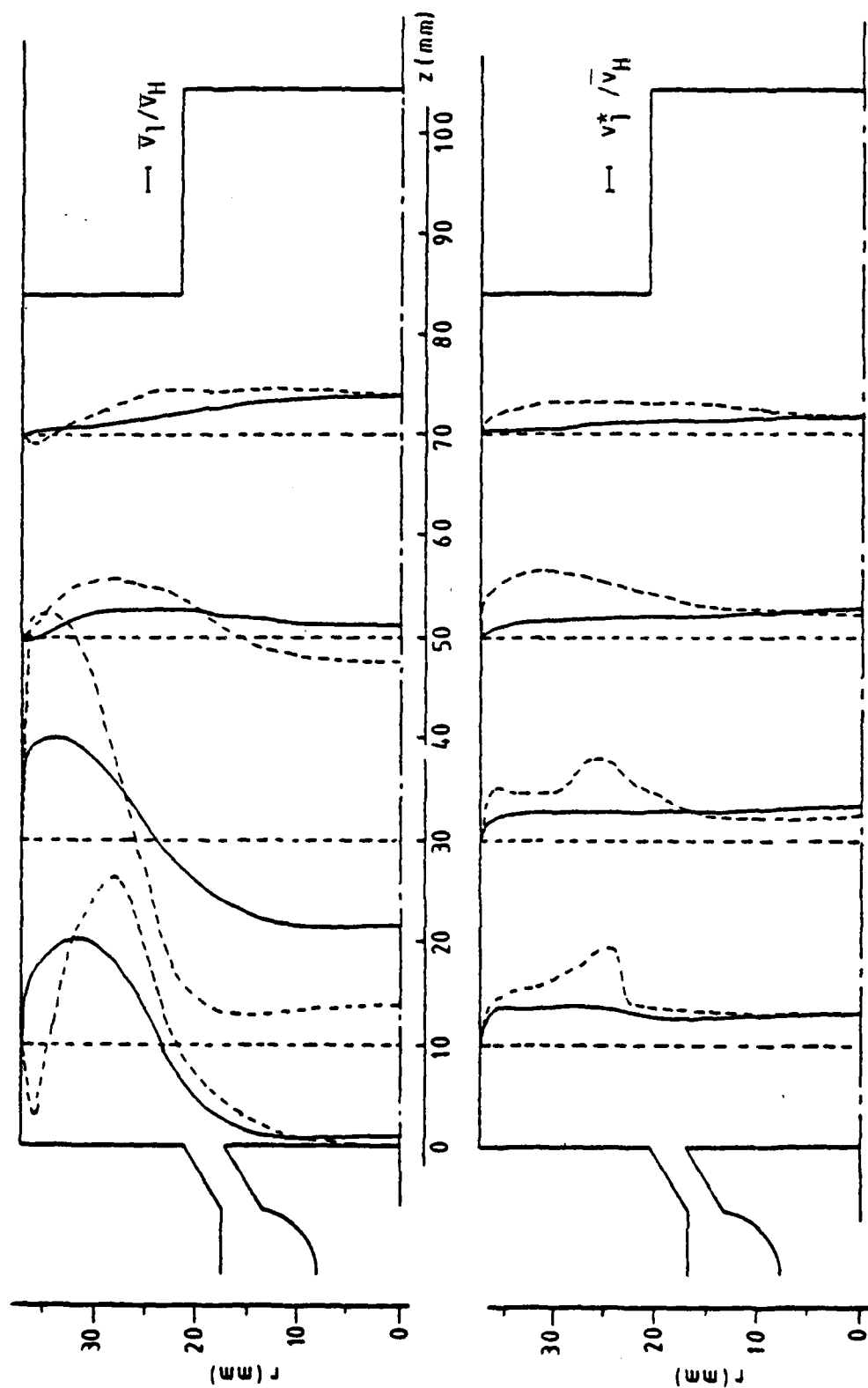


Fig. 26 Measured (---) and calculated (—) mean and turbulent axial velocities

at 144° for case 3

cor'd....

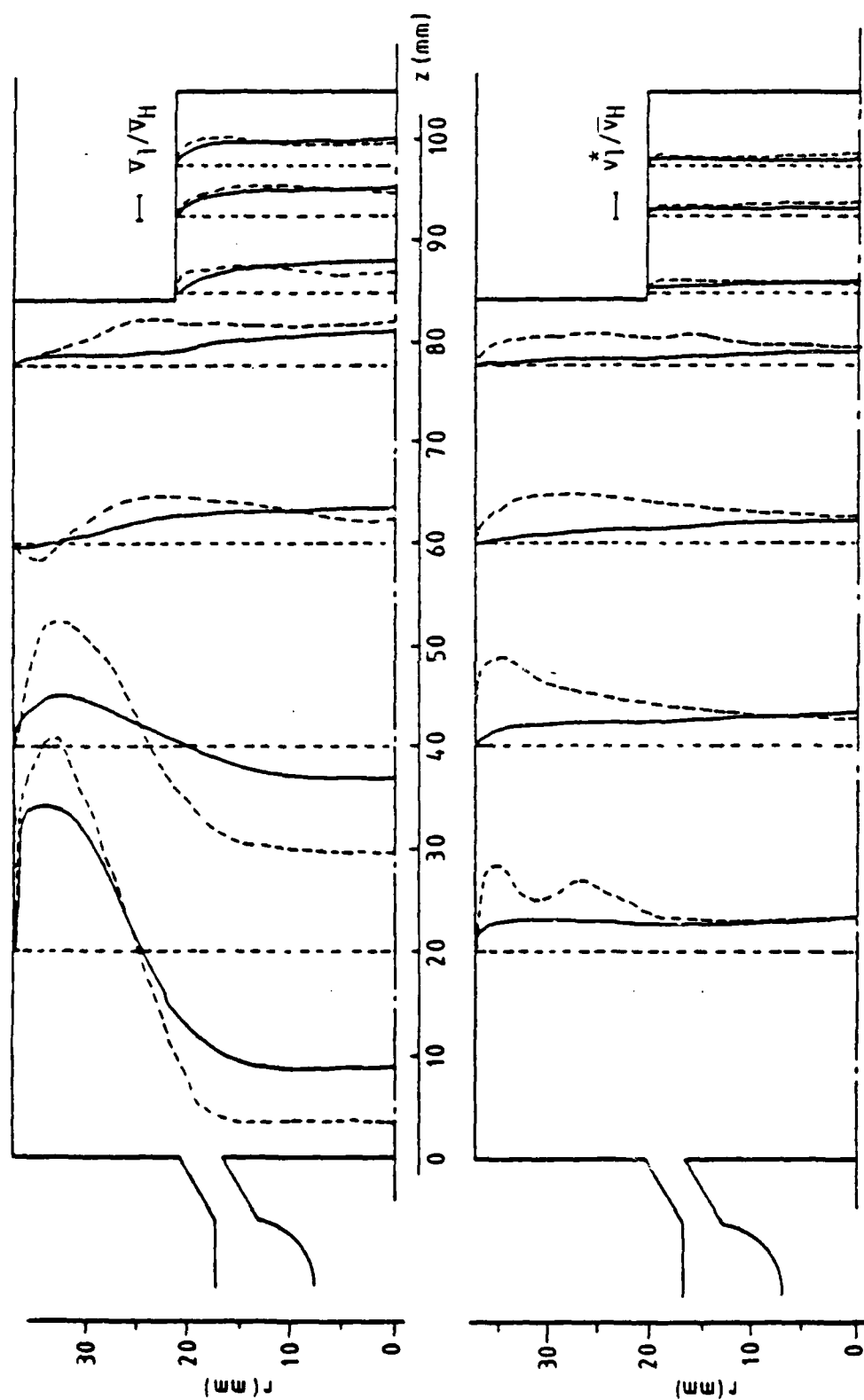


Fig. 26 Measured (---) and calculated (—) mean and turbulent axial velocities

at 144° for case 3

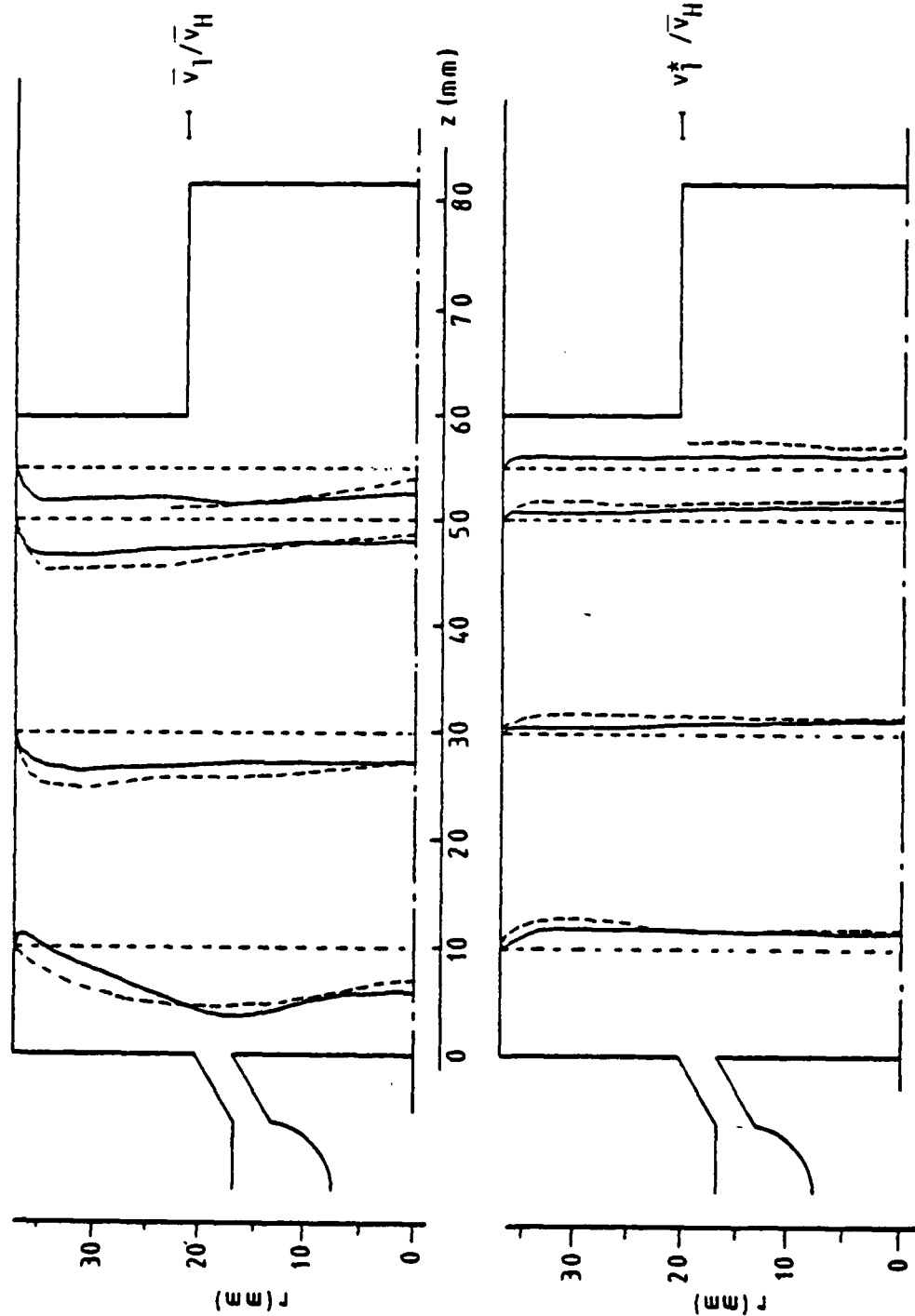


Fig. 27 Measured (---) and calculated (—) mean and turbulent axial velocities

at 270° for case 3

DATE
FILMED
-8